UNIVERSITAT POLITÈCNICA DE CATALUNYA

UNIVERSITAT DE BARCELONA

Projecte Final d'Estudis
MÀSTER
EN
ENGINYERIA BIOMÈDICA

EB

Validation of the simulation code PRIMO for external radiotherapy

Barcelona, Setembre de 2014

Autor: Borja Mercadal Cavaller
Directora: Dra. María Amor Duch

Realitzat a: INTE (UPC)

Summary

Cancer is one of the leading causes of death around the world and the number of patients is expected to increase in the next years. Most of the cancer patients are treated with radiotherapy for at least a part of their treatment. The success of a radiation therapy treatment lies on its correct planification and the accurate prediction of dose distribution in the patient.

These dose distributions are generated using treatment planning systems. Analytical algorithms are commonly used despite more accurate results can be achieved using Monte Carlo based algorithms due to the long calculation times required by them. In 2013 a new Monte Carlo based algorithm, PRIMO, was developed. In this program, based on PENELOPE, several variance reduction techniques have been included in order to speed up the calculations as well as a graphical user interface has been designed to make it user friendly.

This work will help to validate the simulation code PRIMO. The validation of a treatment planning algorithm involves many different tests, among them, a basic validation of computed doses compared to measurements in water, as well as the verification of its dosimetric accuracy in complex situations.

The aim of this work is to investigate the performance of the PRIMO code, in particular to study its dosimetric accuracy in complex situations such as the presence of materials different than water (lung and bone) and when computing the dose within the first millimeters of the patient. This aim was translated into a set of computational experiments performed on simple geometrical phantoms as well as on computerized tomography

images.

Results showed that the algorithm allows to obtain accurate results in water phantoms, as well as in regions susceptible to errors like the build up region and regions with material heterogeneities.

Contents

Chapter 1

Introduction

Cancer is a generic term for a large group of diseases that can affect any part of the body. Other terms used are malignant tumours and neoplasms. One defining feature of cancer is the rapid creation of abnormal cells that grow beyond their usual boundaries, and which can then invade adjoining parts of the body and spread to other organs. This process is referred to as metastasis. Metastases are the major cause of death from cancer. Cancer is a leading cause of death worldwide, accounting for 8.2 million deaths in 2012 and it is expected that annual cancer cases will rise from 14 million in 2012 to 22 within the next two decades [1].

Cancer treatment requires a careful selection of one or more intervention. Surgery, radiation therapy and chemotherapy are the standard methods of cancer treatment and the goal is to cure the disease or considerably prolong life while improving the patient's quality of life. At present over half of the cancer patients who are cured benefit from radiation therapy and, in industrialized countries, about 70% of cancer patients are referred to a radiation therapy department for at least part of the treatment. The majority is treated with 'conventional' photon beam therapy, which for that reason remains the reference radiation treatment modality[2].

A radiation therapy treatment requires a previous planning to generate beam shapes and dose distributions with the aim of maximizing the dose in the tumor region and at the

same time minimize the dose in healthy tissues. These dose distributions are generated using dose calculation algorithms. The most common algorithms used in hospitals are the analytical which provide a reasonable accuracy requiring an acceptable amount of time. A much greater accuracy can be reached using Monte Carlo algorithms but those algorithms require long simulation times and also entail a difficulty preparing, executing and analyzing a simulation.

Recently (2013) a Monte Carlo based algorithm, PRIMO, has been developed. This software combines a graphical user interface and a computation engine based on the Monte Carlo code PENELOPE. In addition a set of variance reduction techniques have been developed in order to increase the speed.

In this work a set of computational experiments has been run in order to investigate the performance of the algorithm in selected problems of interest from a dosimetric point of view.

Chapter 2

Background

2.1 Radiotherapy basis

In radiotherapy (RT) ionizing radiation is used to damage the DNA of cancerous cells by either direct or indirect ionizations of the atoms which make up the DNA chain. The aim is to kill all viable cancer cells by delivering as much as possible dose to the target while minimizing the dose to surrounding healthy tissues.

In direct action the radiation interacts directly with the DNA of the cell. The atoms of the DNA may be ionized or excited through Coulomb interactions, leading to the chain of physical and chemical events that eventually produce the biological damage. In indirect action the radiation interacts with other molecules and atoms, mainly water, and produce free radicals, which can, through diffusion in the cell, damage the DNA structure. In interactions of radiation with water, short lived yet extremely reactive free radicals such as H_2O^+ (ion water) and $OH\bullet$ (hydroxyl radical) are produced. The free radicals in turn can cause damage to the DNA chain [2].

RT has two main modalities: external beam RT and brachytherapy. In external beam RT the radiation source is external to the patient while in brachytherapy radioactive seeds are placed inside the patient in direct contact with the tumor. Different types of particle RT also co-exist nowadays and the appropriate choice among them depends on many

factors. Tumors can be treated with electrons, photons, protons or heavier ions beams. We will focus on external beam RT, specifically in photon beam RT.

2.1.1 Megavoltage (MV) photon beams

Photon RT beams are commonly generated by modern linear accelerators (linacs) which are accelerators that accelerate electrons to kinetic energies from 4 to 25 MeV using non-conservative microwave RF fields. These electron beams are decelerated in special high density targets. Most of the electron's kinetic energy is transformed in the target into heat, and a small fraction of the energy is emitted in the form of X ray photons, which are divided into two groups: characteristic X rays and bremsstrahlung X rays [2].

In order to generate clinical photon beams, besides the x-ray target, several components that influence the production, shaping, localizing and monitoring of the photon beams are required. All these features are contained in the linac head or gantry (Diagram of the linac head structure is shown in figure 2.1).

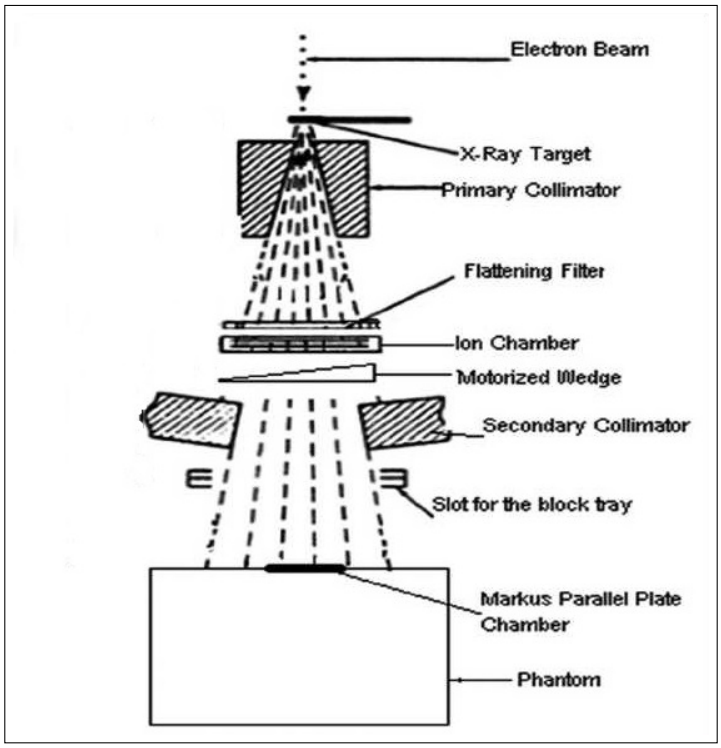

Figure 2.1: Schematic representation of the basic components of a linac treatment head

A photon beam propagating through air or a vacuum is governed by the inverse square law; but a photon beam propagating through a phantom or patient,on the other hand, is affected not only by the inverse square law but also by the attenuation and scattering of the photon beam inside the phantom or patient. These three effects make the dose deposition in a phantom or patient a complicated process and its determination a complex task. Figure 2.2 shows a typical dose distribution on the central axis of a MV photon beam. The region between the surface and the dose maximum is referred to as the build-up region. In this region dose deposition presents a sharp gradient due to the secondary charged particles released by photon interactions that have a finite range and deposit their kinetic energy in the media.

Since the skin dose in treatments of deep-seated tumors may be the limiting factor in the delivery of high tumor doses, a good estimation of the dose distribution in the build-up zone should be done. However, due to the sharp gradient there is an inherent difficult to measure in this region being extrapolation chambers the reference detectors [3].

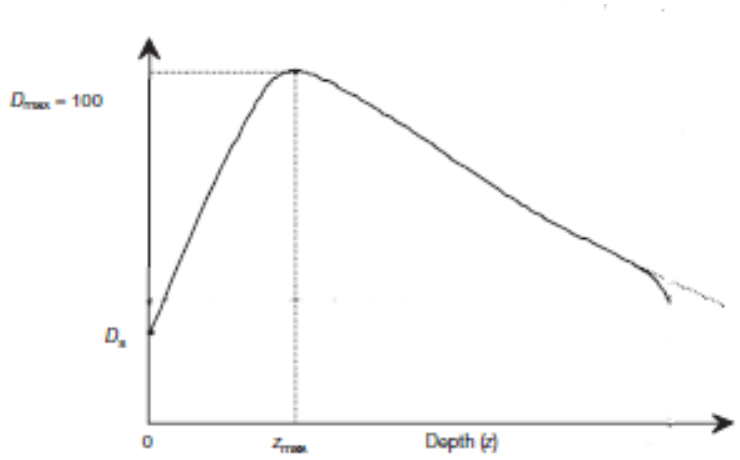

Figure 2.2: Dose deposition from a MV photon beam in a patient. D_s is the surface dose, D_{max} is the dose maximum often normalized to 100, resulting in a depth dose curve referred to as the percentage depth dose (PDD) distribution. The region between $z = 0$ and $z = z_{max}$ is referred to as the dose buildup region.

2.2 RT treatment planning

In a RT treatment planning models of patient anatomy and tumor targets are taken, usually by CT images. The aim is to generate beam shapes and dose distributions with the intent to maximize tumor control and minimize normal tissue complications. This process involves many steps and as a result machine instructions to deliver the treatment are obtained and also the expected dose distribution in the patient, which allows to quantify the tumor control probability (TCP) and the normal tissue complication probability(NTCP).

Dose calculation algorithms are integrated in treatment planning systems (TPS) to obtain the dose distributions within the patient. For clinical applications the most common dose calculation algorithms used are analytical. Several approximations in the dose calculation procedure allow these algorithms to provide dose distributions in clinically acceptable timescales. Usually dose calculations are based on water-equivalent properties and elemental compositions of each material are disregarded, therefore analytical dose calculation algorithms provide reasonable accuracy in water-like tissues but the reliability of predicted dose distributions in the patient might be questioned when the radiation beam is traversing complex tissues heterogeneities.

Many different analytical dose calculation algorithms are currently commercially available, and usually a commercial TPS includes several dose calculation options. Some examples of current TPS and the corresponding options are [4]:

- Varian Eclipse TPS:
  - Advanced Dose Calculation algorithm, Acuros XB.
  - Anisotropic Analytical Algorithm.
  - Single pencil-beam convolution.
- Nucletron Helax-TMS TPS:
  - Collapsed cone.
  - Pencil-beam convolution.

- CMS XiO TPS:
  - Multigrid superposition/convolution.
  - Fast Fourier transform convolution.

Analytical dose calculation algorithms are usually validated using Monte Carlo (MC) simulations and experimental measurements. MC technique for the simulation of the transport of electrons and photons though bulk media consists of using knowledge of the probability distributions governing the individual interactions of electrons and photons in materials to simulate the random trajectories of individual particles. One keeps track of physical quantities of interest for a large number of histories to provide the required information about the average quantities [5]. A random number generator is used to sample the interactions experienced by a particle in chronological succession

As a technique for calculating dose in a patient the underlying physical basis is much simpler in concept than analytic algorithms because the MC method consists of a straightforward simulation of reality and does not involve complex approximations nor models of dose deposition, but only a knowledge of the physics of the various interactions defined as cross sections. MC simulations take into account the specific properties of each material and provide highly accurate dose-distributions, whose accuracy is limited by the number of histories simulated.

The development of efficient computation code and the advances in computer processor technology in recent years, have significantly enabled applications of the MC method in radiation therapy. These advances have motivated several major treatment planning system vendors to embark upon the path of MC techniques. Several MC algorithms for photon, electron and/or proton have already been released or are currently in the process of being released. Some examples for photons and electrons are the PEREGRINE system, the series of codes based on the Voxel Monte Carlo (VMC) (XVMC, VMC++), the dose planning method (DPM) as well as the recently developed PRIMO[6].

2.3 Uncertainties in RT treatment planning

Some studies indicate that at least a 7% difference in dose delivered is manifested in the patient's response to radiation treatment and is detectable clinically by a radiation oncologist [7]. These differences can lead either to a decrease of the TCP, due to an underdosage of the target volume, or an increase in the NTCP, due to an overdosage of healthy tissues or organs at risk. Moreover, several studies have shown that 5% changes in dose can result in $10-20\%$ changes in TCP, or up to $20-30\%$ changes in NTCP.

According to the ICRU, the overall uncertainty in the delivered dose to the patient should not be greater than 5% [8]. Yet previous to the statement of a dose accuracy goal for a RT planification algorithm, it must be taken into account the uncertainties associated to the dose delivered to patient due to all the steps within the dose determination process. Table 2.1 summarizes the estimates from the different sources of error during a complete treatment procedure [7]. Note that nowadays an uncertainty associated to the dose calculation algorithm of 2% or above suppose an overall uncertainty of about 5% or larger.

2.3.1 Evaluation of differences between measurements and dose calculations

When differences between dose calculations and experimental measurements are evaluated, one cannot make simple statements about criteria of acceptability. For instance in regions with low dose gradient it is sufficient to evaluate the dose deviation independently of the spatial consideration while for high dose gradient areas differences on dose may be very large and sensitive to geometric uncertainties. Thus for these regions a better approach is to quantify dose differences as distance to agreement [9]. For this reason it is also commonly used the gamma analysis. Otherwise,when comparing dose profiles is commonly used the beam penumbrae, which is defined as the distance between 80% and 20% of the center axis dose.

Source of uncertainties	Uncertainty at Present (%)	Uncertainty in Future (%)
Dose at the calibration point in water	2.5	1.0
Additional uncertainty for other points	0.6	0.3
Beam monitor stability	1.0	0.5
Beam flatness	1.5	0.5
Patient data	1.5	1.0
Patient set up and organ motion	2.5	2.0
Overall (excluding dose calculation)	4.3	2.5
Dose calculation algorithm (multiple levels)	1.0/2.0/3.0/5.0	1.0/2.0/3.0
TOTAL	4.4/4.7/5.2/5.6	2.7/3.2/3.9

Table 2.1: Estimates of dose uncertainties from the different error sources in absolute dose in the patient for the complete treatment procedure using megavoltage photons. Present values and a prediction of future values. (From AAPM REPORT NO. 85 [7])

The gamma factor, or gamma evaluation method, was first introduced by Low et al.in 1998 [10]. The object of this method is to combine the dose-difference criterion and the distance-to-agreement (DTA) criterion when comparing two distributions.

The method consists on a comparison in the four dimensional dose-position vector space. the points to be compared are $(\boldsymbol{r_c}, D_c)$ and $(\boldsymbol{r_m}, D_m)$ being $\boldsymbol{r}$ the 3-dimensional space coordinate and D the dose at each point.

For all points $(\boldsymbol{r_c}, D_c)$ the difference between measured an calculated dose $\Delta d(i) = D_m(i) - D_c$ is determined, as well as the distance between the points $\Delta s(i) = r_m(i) - r_c$. The Γ value is found then by scaling with the dose difference and DTA tolerances ΔD and ΔS.

$$\Gamma(i) = \sqrt{\left(\frac{\Delta d(i)}{\Delta D}\right)^2 + \left(\frac{\Delta s(i)}{\Delta S}\right)^2} \tag{2.1}$$

And finally the γ index is evaluated as

$$\gamma = min\left[\Gamma(i)\right] \tag{2.2}$$

All points with $\gamma < 1$ are within the acceptance criteria.

Region	Homogeneous, simple geometry	Complex geometry (wedge, inhomogeneity asymmetry, blocks, MLC)	More complex geometries
Central beam axis data- high dose, low dose gradient	2 %	3 %	4 %
Build up region of central axis beam, penumbrae region of the profiles-high dose, high dose gradient	2 mm or 10 %	3 mm or 15 %	3 mm or 15 %
Outside central beam axis region- high dose, low dose gradient	3%	3 %	4 %
Outside beam edges- low dose, low dose gradient	30 % (3 %)	40 % (4 %)	50 % (5 %)
Radiological width- high dose, high dose gradient	2 mm or 1 %	2 mm or 1%	2 mm or 1 %
Beam fringe- high dose, high dose gradient	2 mm	3 mm	3 mm

Table 2.2: Tolerances for the dose deviations and distance to agreement for different regions in a photon beam.From [9]

In this work the obtained results will be evaluated by either the gamma test, the comparison of beam penumbrae or dose deviations.

Some tables of tolerances or expectations have been presented. An example of a criterion for acceptability based on different tolerances for different regions is presented in table 2.2, from the European Society for Radiotherapy and Oncology (ESTRO)[9].

Although a given tolerance may be assigned to each point value comparisons, the acceptance criteria has to be not based on the strict compliment of that tolerance at each point. A more suitable way to compare calculations and measurements is to analyze the deviations statistically.

Chapter 3

Aim and main tasks

The aim of this work is to investigate the performance of the MC based code PRIMO for external radiotherapy in terms of dosimetric accuracy. Specifically a dosimetric accuracy assessment has been performed for a Varian Clinac 2100 C/D (Varian, Palo Alto, CA) linac in photon mode. This has been done by benchmarking the results obtained in simulations with experimental measurements obtained in a clinical environment.

The process focused in three main tasks:

- Dose in water phantoms. First a fundamental validation of the code and the main basic simulation parameters has been done. Then the dosimetric accuracy of the code has been tested in water phantoms for different beam energies and field sizes.
- Dose in the build-up region. Dose calculation in the build-up region is inherently difficult for any algorithm. Therefore special attention has been addressed to this zone and different beam energies have been simulated.
- Dose in heterogeneous phantoms. Dose calculations in phantoms with lung and bone heterogeneities have been studied for different field sizes.

Chapter 4

Materials and Methods

4.1 PRIMO

PRIMO is a computer software, recently developed (2013), that simulates clinical linear accelerators (linacs) and estimates absorbed dose distributions in water phantoms and computerized tomographies (CT). It combines a graphical user interface and a computation engine based on the MC code PENELOPE [11][12]. PENELOPE is a MC based code that allows the simulation of the electron-photon transport within a wide range of materials between energies from few hundred eV to GeV in complex geometries.

MC method applied to the simulation of radiation transport in radiotherapy treatments provide accurate results. General purpose MC codes present two main limitations for the implementation in clinical routine: long simulation times are required to reduce statistical uncertainty to acceptable levels, and these codes also entail a difficulty and effort preparing, executing and analyzing a simulation.

Simulation of a medical linac and computation of the absorbed dose distribution in patients require coding the linac geometry, which is a tedious and error-prone task. PRIMO generates the necessary input files for simulating a variety of Varian and Electa linacs with the MC code PENELOPE and computes dose distributions in water phantoms and CTs[13].

In order to increase the simulation speed, the authors developed a set of variance-reduction techniques (see appendix A). All these features and functionalities are combined in PRIMO under a friendly graphical user interface, which includes various tools for analyzing and representing generated data.

4.1.1 Simulation setup in PRIMO

Once a simulation project is started, in first place PRIMO allows to choose between the different linac models implemented and two operation modes (electron or photon). The whole simulation is divided in three segments s1, s2 and s3 that have to be simulated in sequential order, however they can be grouped. This means they can be simulated individually (s1,s2,s3), grouped in a single simulation (s1+s2+s3) or in smaller groups for example simulating s1+s2 first and then s3. After each simulation a phase-space file (PSF), a file containing information of each one of the particles in the simulation (type of particle, energy, position and direction), is generated. This means that when only segment s1 is simulated, a PSF containing all the particles that have reached the downstream end of the upper part of the linac is obtained as a result.

The segment s1 corresponds to the upper part of the linac (target, flattening filter, primary and secondary collimators and ionization chamber). Before the simulation of this segment the nominal energy of the beam has to be selected, furthermore some beam parameters can be tuned. These parameters are: initial electron energy, energy at full width half maximum (FWHM) and FWHM of the focal spot size (the last two parameters assume a Gaussian distribution for the energy and for the radial distribution of the electrons). According to the authors the default beam parameters that are suggested in the program for each nominal energy have been tuned for Varian linacs to reproduce experimental results.

Segment s2 simulates the movable collimators (jaws) and the multileaf collimator. When simulating this segment the program allows to define the field size and position as well as gantry, collimator and couch angles, and isocenter position. Multileaf collimators or electron applicators can also be selected in this segment.

Segment s3 is the part dedicated to the dose estimation. There are two geometry models available for dose calculation in PRIMO, namely, an homogeneous water phantom and a CT volume. When simulation is done using a water phantom, the program allows to choose the size of this phantom and the bin size in the different directions x, y and z. Otherwise, when working with a CT, a CT volume (as a set of DICOM images) must be imported. Once the images are imported each slice is converted to a size of 256 x 256 pixels and the CT volume is used to generate a voxelized simulation geometry. This geometry consists of a set of material and mass density value pairs.

The volume segmentation is done by assigning a material to a CT number or Hounsfield units (HU) interval. PRIMO allows to include up to 10 different materials from a list of 40 and change the CT number interval for each material included. As well as assigning a material, a density must be attributed to each voxel too. This is done by using a CT scanner calibration curve, a curve that associates each HU to a density. A default curve is provided with PRIMO, but it is possible to edit the default curve and create a custom one.

As already mentioned PRIMO has several variance-reduction techniques implemented to increase the speed of the simulations (See appendix A). During the simulation setup some of these techniques can be adjusted: when simulating linac parts (s1 and s2), one can choose between using either splitting roulette, rotational splitting or no splitting in this segments. According to the authors, for nominal energies below 15 MV in photon mode it is recommended to use splitting roulette, while for nominal energies above 15 MV rotational splitting is usually more efficient. Otherwise when simulating the phantom or CT segment (s3) one may apply a splitting factor. In this case authors suggest to use a factor of 100. Other variance-reduction techniques included in PRIMO have been previously tuned up by the authors and the program does not allow the user to make any change on them.

4.1.2 Computational tools

The code have been tested by the authors using a computer with a 64 bits processor, with a 64 bits Windows as operating system. They recommend 1 GB RAM per computing core. PRIMO can distribute the simulation among several cores up to 24. This means the more cores the computer have the more the simulation times are decreased.

In this work two different computers have been used:

- 64 bits processor Intel ® Core^{TM} 2 duo E8500 at 3.16 GHz, 4 GB RAM and a 64 bits Windows 7 as operative system.
- 32 bits processor Intel ® Core^{TM} i3-2100 at 3.10 GHz, 4GB RAM and a 32 bits Windows 7 as operative system.

4.2 Experimental measurements

Experimental measurements used in this work have been taken from previous works [6]. In all cases detectors were calibrated to yield Dose in water (D_w) regardless of the media they were embedded in. Three different groups of experimental measurements were used in this work.

4.2.1 Radiation dosimeters

Ionization chambers

A ionization chamber (IC) consists of a gas-filled chamber with two electrodes (parallel planes or coaxial cilinders), a voltage potential is applied between the electrodes to create an electric field in the fill gas. When ionizing radiation interacts with the gas pairs of charges are created and the resultant positive ions and dissociated electrons move to the electrodes of the opposite polarity under the influence of the electric field. This movement

generates a current, which is measured by an electrometer.

Different types of IC were used in this work: a 0.35 cm^3 Roos (PTW, Freiburg, Germany), a 0.016 cm^3 PinPoint 31016 (PTW, Freiburg, Germany) and a NACP 2 parallel plate (IBA dosimetry GmbH, Germany). All of them connected to a PTW-Unidos electrometer.

Diode dosimeters

Radiation produces electron-hole pairs in the body of a p-n junction diode. The charges produced in the body of the dosimeter, within the diffusion length, diffuse into the depleted region. They are swept across the depletion region under the action of the electric field due to the intrinsic potential. In this way a current is generated in the reverse direction in the diode which is measured by an electrometer. Diodes are particularly useful for measurement in phantoms, for example of small fields used in stereotactic radiosurgery or high dose gradient areas such as the penumbra region.

Scanditronix PFD-3G diodes were used in this work to measure dose profiles.

Thermoluminiscent dosimeters

Thermoluminiscent materials once exposed to ionizing radiation retain part of the absorbed energy. This energy is subsequently released when the material is heated in form of photons in the ultraviolet spectrum. The emitted intensity of light is proportional to the absorbed dose.

Two types of TLD were used in this work: $^7LiF : Mg, Ti$ (TLD-700, Thermo Fisher Scientific Inc., Erlangen, Germany) and $LiF : Cu, Mg, P$ (TLD-2000F, Conqueror Electronics Technology Co. Ltd., Beijing, China).

Before each irradiation, standard annealing was carried out in a PTW-TLDO oven. For the TLD-2000F, the annealing consisted in 10 min at 240°C; for the TLD-700 detectors, the annealing consisted in 1h at 400°C followed by 2h at 100°C. Readout was carried out

with a Thermo Scientific Harshaw 5500 hot gas reader. The heating procedure for the TLD-2000F consisted in a pre-heating at 160ºC during 10 s, followed by a linear heating rate of $8ºC \cdot s^{-1}$ for 20 s up to a temperature of 250ºC. The readout procedure for TLD-700 included a pre-heating phase at 135ºC and a linear heating rate for 10 s at $25ºC \cdot s^{-1}$, up to 270ºC.

Radiochromic films

Radiochromic films present a linear increase of its optic density as a function of the deposited energy independently of dose rate. Radiochromic film measurments were done with EBT2 radichromic films and Gafchromic EBT radiochromic films (International Speciallty Products, Wayne NJ). EBT radiochromic films from a single batch together with an Epson Perfection 4990 Photo scanner (Seiko Epson Corporation, Nagano, Japan) were used.

Extrapolation chamber

An extrapolation chamber is a type of parallel plane ionization chamber, capable to measure the differential specific charge by varying air mass in the cavity through controlled variations in the electrode separation. These chambers are designed for fields that have a uniform intensity across the area of the parallel plates, but vary sharply in the perpendicular direction. Furthermore their response in the non-equilibrium region has good results. These features allow to obtain accurate measurements in the Build-up region with extrapolation chambers.

Measurements of the collected charge per unit time per unit volume are obtained reducing gradually the distance between plates. A linear regression of electrode separation and collected charge values allows to relate the measurements with the absorbed dose in the region of interest. A PTW-Freiburg NA 30-360 extrapolation chamber together with a Keithley 2400 digital sourcemeter and a PTW-Unidos electrometer were used in this work.

4.2.2 Dose in water phantoms

PDD curves and dose profiles were measured in water for 6 MV and 18 MV photon beams and for several field sizes ranging from 2×2 cm^2 to 20×20 cm^2 from a Varian Clinac 2100 C/D (Varian, Palo Alto, CA) in photon mode. Measurements were performed in Institut Català d'Oncologia Girona (ICOG) using a water phantom of $50 \times 50 \times 50$ cm^3.

PDD curves were measured using Roos IC and PinPoint IC. Due to their physical dimensions, the Roos IC was used for the largest fields (10×10 cm^2 and 20×20 cm^2), whereas the PinPoint 31016 IC was preferred for the smallest fields measurements (2×2 cm^2 and 5×5 cm^2). IC measurements were carried out by the radiophysicists at ICOG. Profiles were measured using Scanditronix PFD-3G diodes.

4.2.3 Dose in the build-up region

PDD curve in the build-up region was measured for 6 MV and 15 MV photon beams with a field size of $10x10cm^2$ in a water equivalent slab phantom made of plastic water^{TM}. Measurements were performed in the Santa Creu i Sant Pau Hospital with a Varian Clinac 2100 C/D in photon mode [14].

PDD curve in this region presents a sharp gradient. This makes difficult to obtain accurate measurements of dose in this region specially in the first centimeter of the curve. For this reason PDD curves measured with different dosimeters were compared with the results obtained with MC taking the extrapolation chamber as a gold standard.

Measurements of this region were done with the PTW-Freiburg extrapolation chamber,and in addition with a NACP 2 IC, an Exradin W1 (Standard Imaging, USA) scintillator detector and EBT2 films. The experimental setup used to measure the dose in the build-up region with the extrapolation chamber is shown in figure 4.1.

Experimental measurements were repeated at least three times in three different days, and the corresponding mean value has been taken as a reference. More details can be found elsewhere [14].

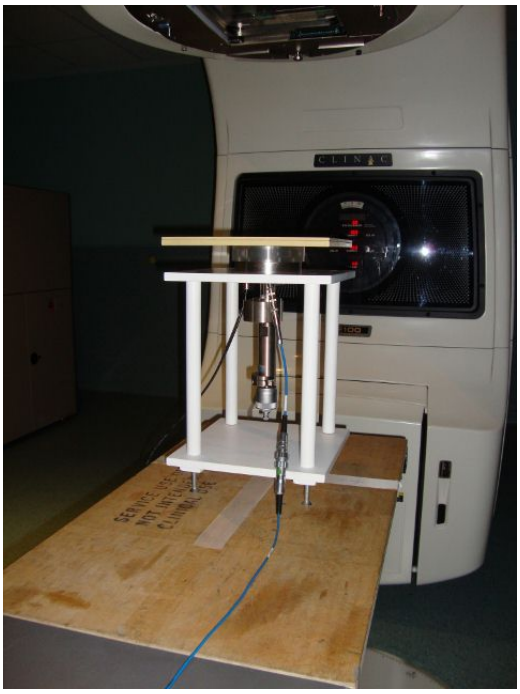

Figure 4.1: Experimental setup used for the measurements in the build-up region with the Extrapolation Chamber.

4.2.4 Heterogeneous phantoms

Two experimental configurations were studied. A water-equivalent slab phantom (PTW RW3, electron density relative to water $\rho_w^e = 1.012$) with a lung-equivalent heterogeneity (Computerized Imaging Reference Systems (CIRS, Norfolk (VA), $\rho_w^e = 0.195$) and the same water-equivalent slab phantom with a bone-equivalent heterogeneity (cortical bone CIRS, $\rho_w^e = 1.779$)

The phantom consisted of $30 \times 30\ cm^2$ slabs with thickness ranging from 0.1 to 5 cm. The experimental configurations consisted on: 5 cm of RW3 followed by 13 cm of lung and then by 10 cm of RW3 and 5 cm of RW3, 10 cm of bone and then 10 cm of RW3 (see figure 4.2). Although the second configuration has no meaning from a clinical perspective (therapy fields would rarely traverse such thickness of cortical bone) it provides a wider region to evaluate the behavior of the algorithm.

PDD's and dose profiles were measured in both experimental configurations for 6 MV

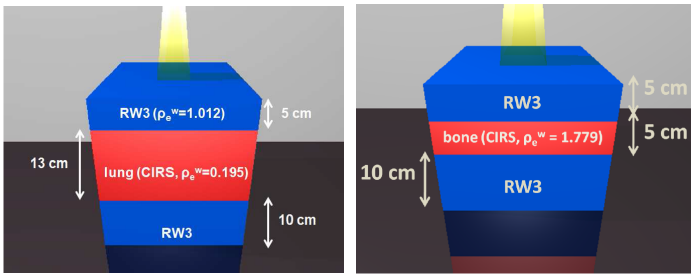

Figure 4.2: Schematic representation of the experimental configurations.

photon beams with field sizes of 2×2, 5×5, 10×10 and. Measurements were performed in ICOG using a Varian Clinac 2100 C/D. Several types of detectors were used to measure dose in these phantoms: IC, thermoluminiscent dosimeters(TLD) and Radiochromic films. The ICs used for this experimental setup were the same as in section 4.2.2.

Parallel IC cannot be used inside tissues other than water without aplying a correction factor from the fluence perturbation caused by the presence of the chamber in the medium. Since such factors were unknown for these IC, only TLDs were used in lung and bone.

Thermoluminiscent materials used have an effective atomic number similar to soft tissue, which minimizes potential perturbation effects when measuring in soft tissue or water. However, especial care must be given in the case of bone. TLD-2000F were used inside the bone-equivalent region while dose measurements in lung were carried with TLD-700.

Several detectors were used at each depth in order to reduce the statistical uncertainty of the results. Likewise, some measurements were repeated up to three times. This, together with the application of individual correction factors and a senstivity stability control, allowed to achieve results with statistical uncertainties of $\pm 1 - 2\%$ in all cases.

Film dosimetry was used for measuring lateral profiles to avoid the influence of the finite detector size and to improve the spatial resolution. Film measurements were carried out by the radiophysicists at ICOG.

4.2.5 Effective point of measurement

When analyzing experimental results one need to consider the finite dimensions of the detector and its material. Thus the effective point of measurement (EPOM) is defined as the point at which the measured dose would arise in the measurement medium in the absence of the probe. According to a theoretical consideration, the shift of the effective point of measurement from the reference point of the detector is caused by a gradient of the fluence of the ionizing particles. It has been shown that the value of the EPOM depends on the construction of the detector, but remains invariant under changes of radiation quality and depth [15]. Other disturbances, which do not belong to the class of 'gradient effects', are not corrected by shifting the effective point of measurement.

Generally the EPOM is assumed to be at the center of the sensitive region of the detector, scaled by the physical density and is given in g/cm^2. Table 4.1 shows the EPOM considered for the different detectors used in the experimental measurements related to the build-up region. In the rest of the experimental measurements the EPOM was assumed to be negligible.

detector	EPOM (g/mm^2)
PTW NA-30-360	0.069
NACP2	0.6
EBT2	0.1215
EXRadin W1	0.8

Table 4.1: Effective points of measurement considered for the detectors used in the experimental measurements of the build-up region

4.2.6 Dose in medium/dose in water

As we said all detectors used were calibrated to yield dose in water (D_w) regardless of the media they were embedded in. However results obtained after dose tallying with the MC code are referred to dose in medium (D_m) at the point/voxel in which dose is calculated.

Therefore in order to compare MC results with experimental data dose must be expressed in the same medium. The question of which quantity should be adopted for comparison purposes is still under debate, and there are strong arguments both for using D_m or D_w [16].

Using Bragg–Gray cavity theory, the absorbed dose to water is related to the absorbed dose to medium by [17]

$$D_w = D_{med} s_{w,med} \tag{4.1}$$

where $s_{w,med}$ is the unrestricted water-to-medium mass collision stopping power ratio averaged over the energy spectra of primary electrons, $(\Phi_E)_m$. The so-called primary electrons do not include knock-on electrons or δ-rays, as their contributions to energy deposition are accounted for in the unrestricted stopping powers. The stopping power ratio averaged over the primary electron spectrum is calculated using

$$s_{w,med} = \frac{\int_0^{E_{max}} (\Phi_E)_m (S/\rho)_w dE}{\int_0^{E_{max}} (\Phi_E)_m (S/\rho)_{med} dE} \tag{4.2}$$

where $(S/\rho)_w$ and $(S/\rho)_{med}$ are the unrestricted mass collision stopping power for the water and transport medium respectively, and E_{max} is the maximum energy in the $(\Phi_E)_m$ distribution.

To evaluate the Bragg–Gray stopping power ratio for photon beams, knowledge of the electron fluence in the media is required. Presently, only MC-based dose calculation algorithms are capable of determining this quantity.

In this work, before comparing MC with experimental results related to dose calculations in presence of heterogeneities, doses have been converted to D_w applying (4.1) using the water medium stopping-power ratios calculated by Fernandez-Varea et al.[16]:

$$S_{w,bone} = 1.117$$

$$S_{w,lung} = 0.998$$

4.3 Dosimetric assessment of PRIMO

As mentioned in chapter 3, the dosimetric accuracy assessment of PRIMO was done in different stages, using water phantoms and CT images of heterogeneus phantoms. Since all experimental measurements were done using a Varian Clinac 2100 C/D linac in MV photon beam mode all the simulations were done using this model.

4.3.1 Dose in water phantoms

The default parameters of the primary electron beam for Varian linacs have been tuned by the authors. However before starting with the dosimetric assesment of PRIMO a relatively short test was run to check the suitability of the suggested parameters. It consisted on simulations for two beam energies (6MV and 18MV), using different field sizes ranging from 2×2 cm^2 to 20×20 cm^2 from a Varian Clinac 2100 C/D in photon mode.

Calculations of dose in water phantoms were evaluated for a $50 \times 50 \times 50$ cm^3 homogeneous water phantom. Results and experimental measurements of the PDD curves were compared in terms of dose difference and distance to agreement. The gamma factor was also calculated. Since the aim of this test was to check the energetic parameters of the electron beam, dose profiles were not evaluated.

Simulations were run in relatively short times, using the rotational splitting technique for the 18 MV beam and the splitting roulette for the 6 MV beam. To speed up the dose calculations, a splitting factor of 20 were used in the water phantom. Bin sizes used for the dose tallying in the phantom were 0.2 cm in z direction (beam direction) and 0.25-0.50 cm in x and y directions (perpendicular to the beam direction). Furthermore an average statistical uncertainty of 2% in dose tallying was required on each simulation.

Once the suitability of the electron beam parameters had been checked, calculations of dose in water phantoms were evaluated for a $50 \times 50 \times 50$ cm^2 homogeneous water phantom. Again, two beam energies (6MV and 18 MV) and several field sizes ranging from 2×2 cm^2 to 20×20 cm^2 from a Varian Clinac 2100 C/D in photon mode were simulated. Simulation

results and experimental measurements of PDD and profile percentage dose (PPD) were benchmarked in terms of dose difference and distance to agreement. Differences were also evaluated using the gamma analysis and differences in beam penumbrae were evaluated for experimental and simulated profiles.

As in the first set of simulations, the rotational splitting technique was used for simulations with 18 MV beam and the splitting roulette for the 6 MV beam. A splitting factor of 100 was used when tallying the dose in the water phantom. Bin sizes in this case were 0.2 cm in z direction and 0.25 cm in x and y directions except in simulations with the smallest fields where 0.33 cm in z and 0.2 cm in x and y directions were used. The maximum number of bins is limited to 10^7 in simulations with PRIMO. The maximum allowed number of bins is used in each simulations and different bin sizes are used to increase the number of bins that are traversed by the beam in the smallest fields and thus obtain a higher spatial resolution in results when evaluating dose profiles. The average statistical uncertainty required was set to 2% in dose tallying.

4.3.2 Dose in the build-up region

The build-up region is characterized for a sharp dose gradient, for this reason dose calculation algorithms present the biggest discrepancies between experimental and calculated dose in this region. PRIMO does not allow to simulate geometrical phantoms with materials different than water, nevertheless the available measurements in this region are from a plastic water^{TM} phantom. Due to the sharp dose gradient, results in this region can be very sensitive to a little difference in the effective atomic number or density. Hence a Phase space file (PSF) generated at the at the downstream end of the lower part of the linac by PRIMO was used to tally the dose in a plastic water phantom using the MC code Penelope with penEasy as the main program. To have an adequate spatial resolution, a bin size of 0.02 mm was used in the first milimeter and 0.1 mm in the rest of the phantom. In lateral dimensions the bin size used was 1 cm.

Results obtained were evaluated in terms of dose difference and distance to agreement against experimental measurements from an extrapolation chamber and were also

compared against the results obtained using various dosimeters.

The extrapolation chamber was taken as the gold standard. Nevertheless, an extrapolation chamber is not commonly available moreover measurements with an extrapolation chamber are tedious. For this reason Results have been compared to other detectors with the purpose of analyze if those detectors are suitable to validate the code and if so in which depth ranges can be used.

4.3.3 Dose in heterogeneous phantoms

The geometry of the two experimental setups showed in section 4.2.4 was introduced to the program through CT images of the phantoms. Images were generated on an Optima CT580RT CT scanner (General Electric Healthcare, Fairfield,CT). When simulating with CT images, several potential sources of error play an important role: discrepancy associated to the CT calibration curve, discrepancies associated to the material assignment, discrepancies due to the artifacts arisen from the image acquisition; and, as well as in every simulation, discrepancies associated to the MC algorithm (PSF generation, dose calculation algorithm...)

First, simulations of a 10×10 cm^2 field were run for both geometries. In these simulations the CT calibration curve and the HU to material assignation by default (see figure 4.3)were used. The aim was to analyze the results that would obtain someone without any knowledge of the program only running the simulation with the parameters by default.

After these simulations the CT calibration curve was adjusted to the used CT scanner. Besides only materials present in the geometry were used in the HU to material assignation. MS20 muscle and cartilage (ICRP) were the materials chosen for the density range of the RW3 slab phantom because these materials are those with an effective atomic number most similar than the water among the available materials. Figures 4.4 and 4.5 show the CT calibration curve and the HU to material assigned on each simulation respectively. Various fields between $2x2cm^2$ and $10x10cm^2$ were simulated for each geometry.

Material	Density	CT Range
Air	0.0012	0- 284
Lung (ICRP)	0.3000	284- 545
Adipose tissue	0.9200	545- 806
Soft tissue	1.0000	806-1067
Muscle striated	1.0400	1067-1329
Muscle skeletal	1.0500	1329-1590
Cartilage (ICRP)	1.1000	1590-1851
Inner Bone	1.3000	1851-2112
Bone Compact	1.8500	2112-2373

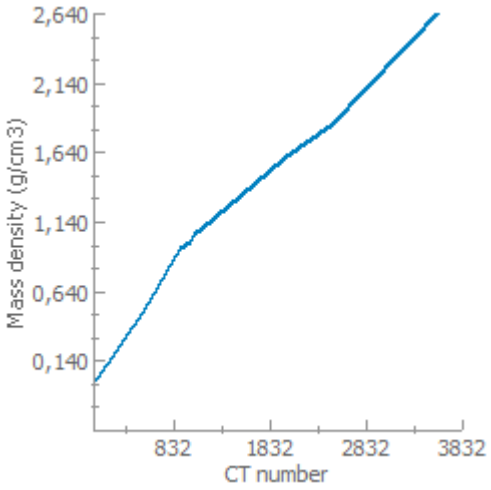

Figure 4.3: HU to materials assignation (left) and CT calibration curve (right) used in the first set of simulations.

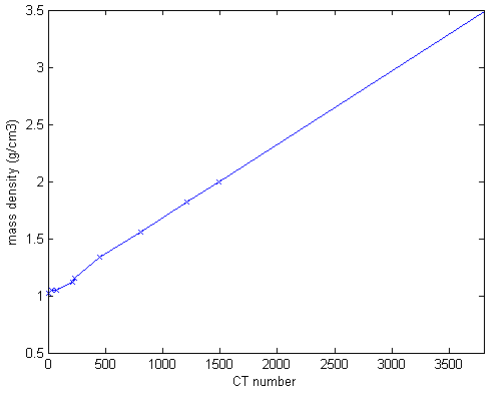

Figure 4.4: CT calibration curve given of the CT scanner used to acquire the images.

Material	Density	CT Range
Air	0.0012	0- 284
MS20 Muscle	1.0000	284-1275
Cartilage (ICRP)	1.1000	1275-1405
Bone Compact	1.8500	1405-2373

Material	Density	CT Range
Air	0.0012	0- 92
Lung (ICRP)	0.3000	92- 396
MS20 Muscle	1.0000	396-1067
Cartilage (ICRP)	1.1000	1067-1702

Figure 4.5: HU to materials assignation used for the bone equivalent heterogeneity phantom(left) and for the lung equivalent heterogeneity phantom (right) in the second set of simulations.

When calculating the PDD, the normalization is referred to the maximum which is in all cases in the first region of the phantom. Thus a correct density and material assignment in this region is critical because the dose calculated in the maximum affects the whole curve. For this reason a simulation of a $5x5cm^2$ was run for the bone-equivalent heterogeneity replacing the MS20 muscle and the cartilage for water in the material list. The aim was to see the effect of the material assignment in this region on the PDD curve.

In all simulations with PRIMO the splitting roulette technique was used, a splitting factor in CT of 100 was set and a statistical uncertainty of 2% was required.

Finally, to analyze the effects of the artifacts generated by the CT image acquisition, the two studied phantoms were also simulated with PENELOPE but in a non-voxelized geometry, modelling the phantom materials according to the atomic composition specified by the manufacturer instead of using the CT material assignment. Using the PSFs generated at the end of the linac by PRIMO in the previous simulations the dose was tallied in these geometrical phantoms. Calculations were done using PENELOPE with PenEasy[18] as the main program. In order to perform a meaningful comparison the bin size used in this calculations was the same as the voxel size of the CT images.

Chapter 5

Results

5.1 Dose in water phantoms

5.1.1 Verification of the electron beam parameters

Results obtained in the initial simulations, conducted to check the suitability of the parameters proposed by PRIMO, were in good agreement with experimental results. Discrepancies were below 2% along the PDD curves except in the first centimeter. In this region higher differences are expected due to the high dose gradient and we have seen in section 2.3 that discrepancies of about 10% are acceptable in this region.

Table 5.1 shows the results of the gamma test and the discrepancies at the maximum of the curve in terms of distance to agreement and dose difference. The percentage of points passing the gamma test is above 99% in all cases except for the 6 MV and $20 \times 20\ cm^2$ beam. Dose differences at the maximum of the curve are below 1% and the distance to agreement in this point is 2 mm or below in all cases also with the exception of the 18 MV and $20 \times 20\ cm^2$ beam where distance is 4 mm. Nevertheless dose difference in this case is also below 1%.

Simulations with wide fields ($20 \times 20\ cm^2$) require a larger number of histories than smaller fields in order reduce the statistical uncertainty at the same level. Thus we see the

higher discrepancies in that cases. However the aim of this first set of simulations was only to check the suitability of the energetic beam parameters before starting the validation of the code. Therefore it was not considered the need to repeat this simulations with a larger number of histories.

The conclusion of this first stage was that the energetic beam parameters were properly tuned up to begin the dosimetric assessment.

	field size (cm^2)	percentage of points passing the gamma criteria (%)	distance between maximums (mm)	difference at maximum (%)
6 MV	2x2	99.33	0	0.0
	5x5	99.32	0	0.0
	10x10	99.66	1	0.34
	20x20	91.64	0	0.0
18 MV	3x3	99.32	2	0.19
	6x6	99.32	2	0.07
	10x10	99.32	2	0.27
	20x20	99.32	4	0.61

Table 5.1: Results obtained in water phantoms for parameter default values and short calculation times.

5.1.2 Evaluation of dosimetric accuracy

PDD curves obtained for 6 and 18 MV photon beams are shown in figures 5.1 and 5.2 respectively. Statistical uncertainties were below 0.5% along the PDD curves in all cases and uncertainties in measurements were below 1%. Discrepancies are below 2% in all cases except in the build up region where dose differences above 10% are only found in the surface of the phantom. It is worth to remind that experimental results in this zone are difficult and their discrepancies might be attributable to the used detector (see next section).

Table 5.2 presents the results of the gamma test as well as the deviations in the dose maximum (dose difference and distance to agreement). The percentage of points passing the gamma test is 99% or higher in all cases.

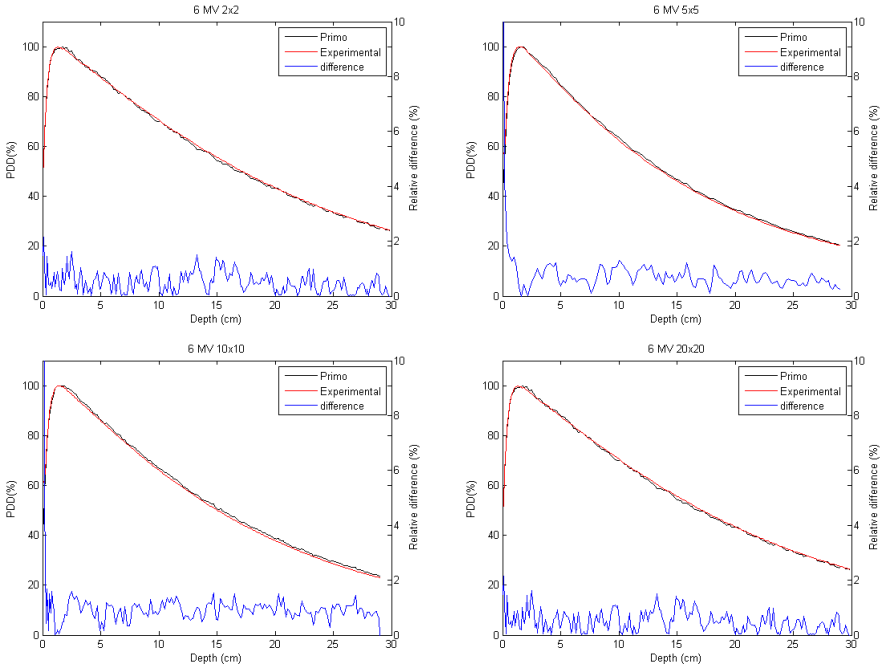

Figure 5.1: PDD curves obtained for 6 MV photon beam using different field sizes in a water phantom.

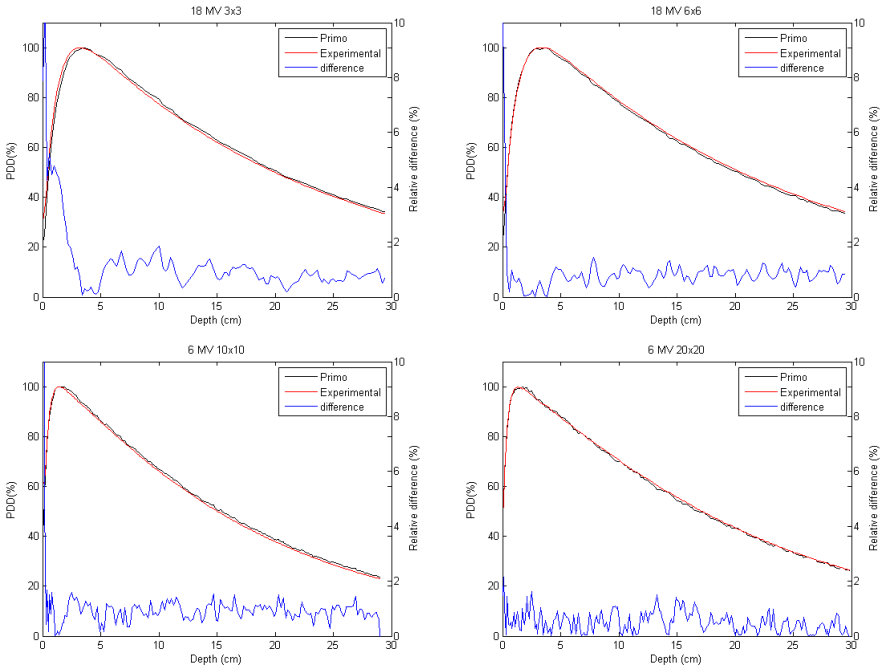

Figure 5.2: PDD curves obtained for 18 MV photon beam using different field sizes in a water phantom.

	field size (cm^2)	percentage of points passing the gamma criteria (%)	distance between maximums (mm)	difference at maximum (%)
6 MV	2x2	99.0	1	0.03
	5x5	99.32	3	0.04
	10x10	99.66	1	0.34
	20x20	99.67	4	0.88
18 MV	3x3	99.32	2	0.71
	6x6	99.32	2	0.34
	10x10	99.32	4	0.97
	20x20	99.32	2	0.29

Table 5.2: Results obtained

Dose profiles are depicted in figures 5.3 and 5.4 for the 6 and 18 MV photon beams respectively. Statistical uncertainties in simulation results were below 1% in all cases and uncertainty in experimental measurements were below 0.5%. Simulations results are in good agreement with experimental measurements in most cases taking into account the large bin size used in the simulations due to the limitation on the number of bins. Largest discrepancies are found in the smallest field sizes. In these cases , despite the maximum number of bins allowed in a simulation has been used, the amount of bins inside the central beam region is still very small.

A comparison of the beam penumbraes in the simulated and measured profiles is shown in table 5.3. Simulations and measurements are in good agreement for the 18 MV beams while differences of 3 and 4 millimeters are found in simulations with 6 MV beams. Nonetheless the focus in this work was on the PDD curves and a smaller bin size as well as a larger number of histories simulated would be necessary to properly evaluate the performance of the code in the case of dose profiles.

The elapsed times for each simulation are listed in table 5.4. In this set of simulations the two different computers available have been used. The number of histories simulated is about 10^8 in all beam configurations. Time required to compute each segment of the simulation is presented separately. Note that in some cases segments S1 and S2 have been calculated together which resulted to be more expensive in computational time than

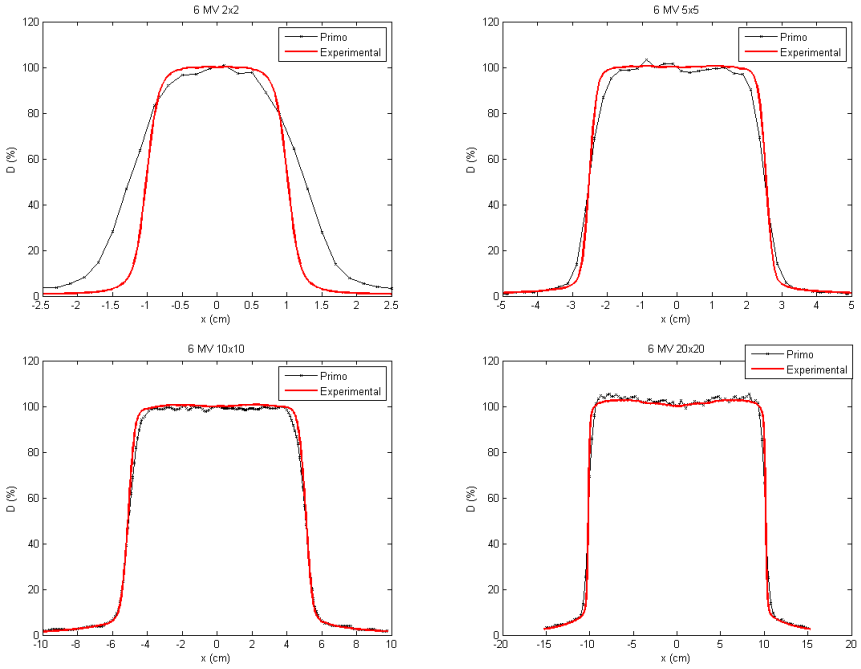

Figure 5.3: Dose profiles obtained for 6 MV photon beam using different field sizes in a water phantom.

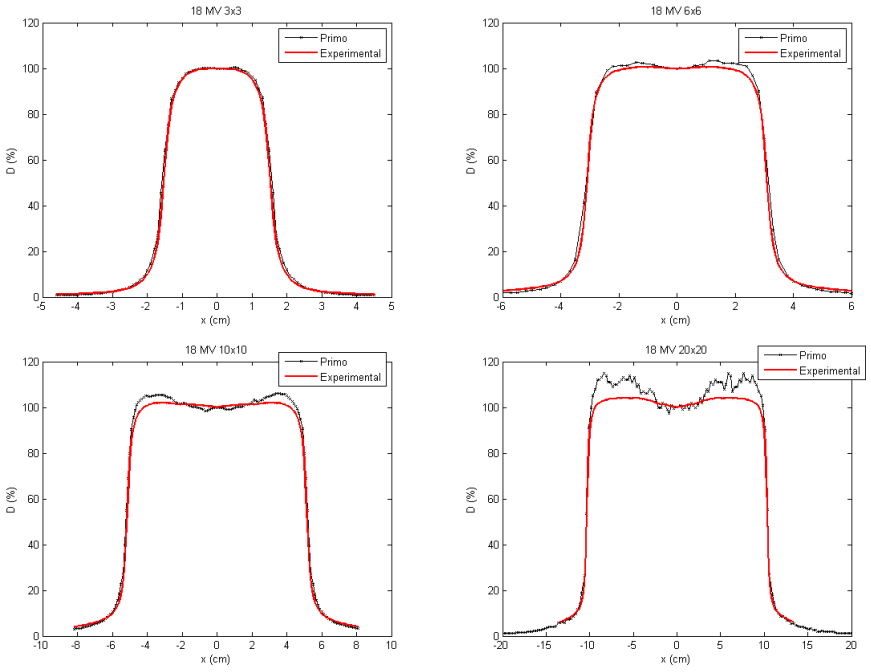

Figure 5.4: Dose profiles obtained for 18 MV photon beam using different field sizes in a water phantom.

Energy	field size	PRIMO	Experimental
6MV	$2 \times 2\ cm^2$	6	3
	$5 \times 5\ cm^2$	7	3
	$10 \times 10\ cm^2$	8	6
	$20 \times 20\ cm^2$	7	3
18 MV	$3 \times 3\ cm^2$	5	4
	$6 \times 6\ cm^2$	5	5
	$10 \times 10\ cm^2$	6	5
	$20 \times 20\ cm^2$	6	6

Table 5.3: Lateral penumbraes in millimeters.

calculating them independently. Calculation times in segment S3 increase as the field size increase. When increasing the field size a larger number of particles is needed to reach the same statistical uncertainty.

Energy	field size	S1	S2	S3
6MV	$2 \times 2\ cm^2$	47.2	2.4	2.0
	$5 \times 5\ cm^2$	35.8	2.9	8.3
	$10 \times 10\ cm^2$	60		12.3
	$20 \times 20\ cm^2$	54.7		61.4
18 MV	$3 \times 3\ cm^{2*}$	33.3	0.5	1.8
	$6 \times 6\ cm^2$	55.8	1.3	5.3
	$10 \times 10\ cm^{2*}$	41.7	1.1	13.2
	$20 \times 20\ cm^{2*}$	36.2		48.6

Table 5.4: Elapsed times for the different simulation segments in hours. Field sizes with a (*) have been simulated using the one core processor computer while the other simulations have been done with the two cores computer.

The results suggest that PRIMO can generate accurate depth dose distributions in water. Results also suggest that the algorithm can also generate reasonably accurate predictions of dose profiles. Nevertheless further investigation is required to study correctly

the performance of the code when predicting dose profiles.

5.2 Dose in the build-up region

Since the the algorithm had not been validated yet in water for 15 MV photon beams a short test was run for this energy in water. A 15 MV photon beam with 10×10 cm^2 field size was simulated in a water phantom and the results were benchmarked with measurements. Figure 5.5 shows the PDD curve obtained. Results were in good agreement with measurements, discrepancies are lower than 2% except in the surface of the phantom and the 99.67% of points passed the gamma test.

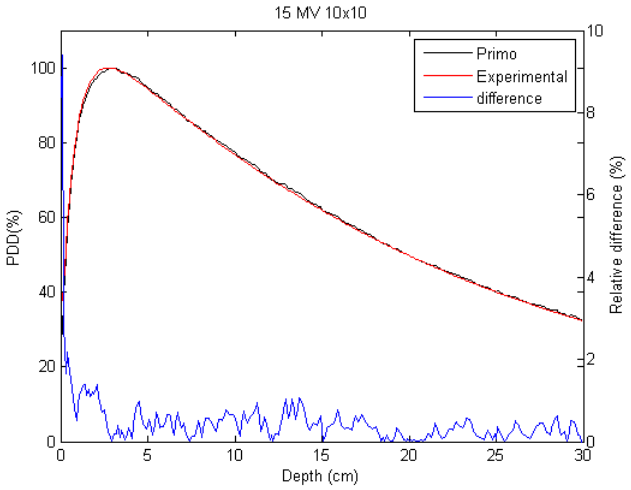

Figure 5.5: Dose profile obtained for 15 MV photon beam using a 10×10 cm^2 field size in a water phantom.

The comparison of the simulation results against extrapolation chamber measurements is shown in figures 5.6 and 5.7. Statistical uncertainties in simulation results were below 1%. Simulation results are in good agreement with the measurements. The average dose difference is 1.9% for the 6 MV beam and 1.7% for the 15 MV beam and the largest discrepancies found are 3.7% and 4.6% for the 6 MV and 15 MV beams respectively. Distance between dose maximums (whose positions are kwnown: 15 mm for 6 MV beam and 30 mm for 15 MV beam) is below 1 mm.

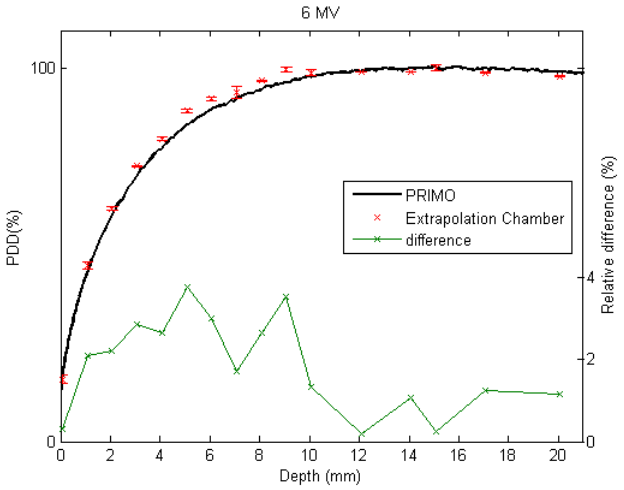

Figure 5.6: PDD's obtained for 6 MV photon beam using the extrapolation chamber and PRIMO

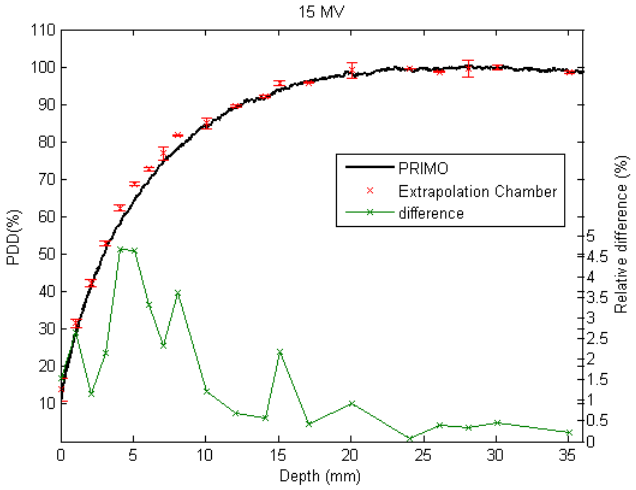

Figure 5.7: PDD's obtained for 15 MV photon beam using the extrapolation chamber and PRIMO

Figures 5.8 and 5.9 show the results obtained with different detectors (IC, scintillation detector and radiochromic films) and also measurements with the extrapolation chamber and the results of the simulations. For the 6 MV beam, in the first 2 mm we found discrepancies of 9.4, 11.1 and 7.8 % between PRIMO and EXradin, NACP2 and EBT2 respectively. For depths over 2 mm the dose difference is below 5% in all cases and below 3% over 5 mm of depth. For the 15 MV beam, discrepancies between PRIMO and

EXradin, NACP2 and EBT2 in the first 2 mm are 5.6, 8.2 and 5.25 % respectively. For depths over 2 mm dose differences are below 4% in all cases.

Results obtained show that PSF files generated with PRIMO allow to obtain accurate results in the build-up region. Otherwise detectors other than the extrapolation chamber, that have been used, are appropriate to obtain measurements in this region for depths over 2 mm and thus can also be used to validate the algorithm in the build-up region within a 5% tolerance.

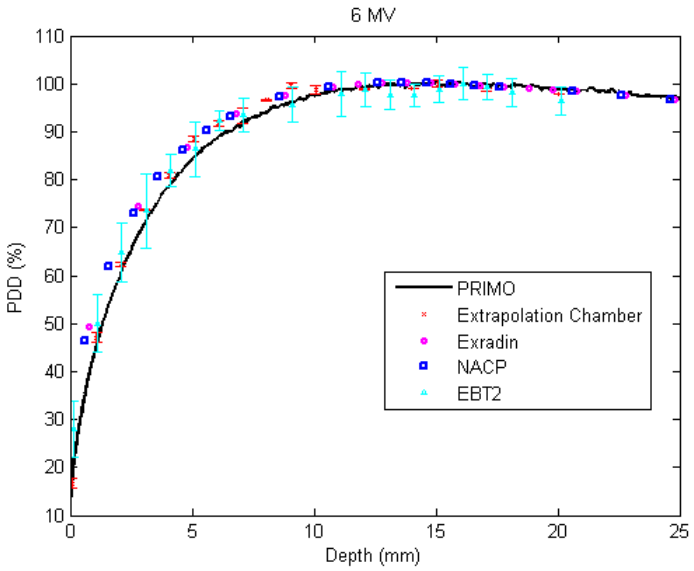

Figure 5.8: PDD's obtained for 6 MV photon beam using different detectors and PRIMO

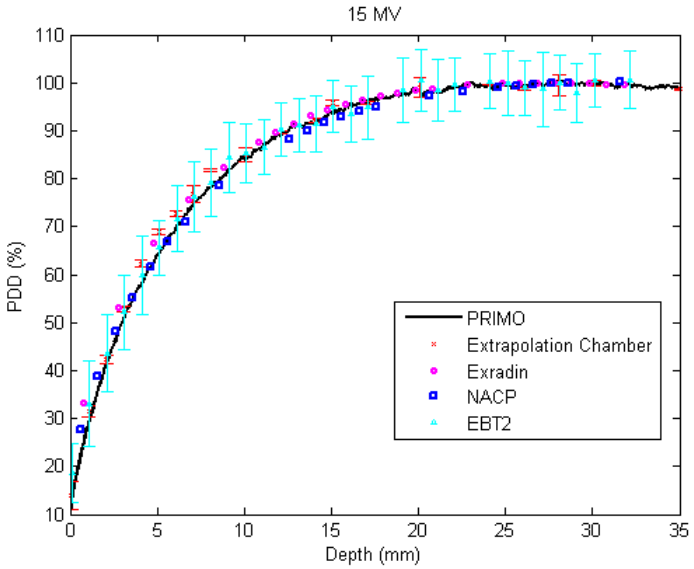

Figure 5.9: PDD's obtained for 15 MV photon beam using different detectors and PRIMO

5.3 Heterogeneous phantoms

5.3.1 Simulations with parameters by default

Figures 5.10 and 5.11 show the results obtained for a $10x10\ cm^2$ field using the calibration curve and the material assignment applied by default by PRIMO. Uncertainties in dose distribution from simulations are below 2% in all points and are not represented. For the phantom with the bone-equivalent heterogeneity we found discrepancies of about 8% in the build up region, which is admissible in this region. In the bone equivalent region dose difference is over 4% in all cases, likewise in the region underneath the heterogeneity where discrepancies are around 5% in all cases.

It is worth to remind that experimental results in the water region were measured with Roos and PinPoint cylindrical ICs that are not suitable for accurate measurements in the build-up region. In addition, the calculation voxel size (about 2.5 millimeters) does not

allow to generate accurate results in zones adjacent to a material change.

Results obtained for the lung-equivalent heterogeneity also present large discrepancies in the build up zone however difference is within the tolerance margins. In this case results in the heterogeneity show a better agreement with experimental results, dose differences are below 4% in all cases. For the region underneath the heterogeneity we found discrepancies around 4% which is the maximum dose difference that can be accepted. It can be observed that the PDD curve in the region of the lung-equivalent heterogeneity presents several abrupt changes in dose. This is due to the material assignment that causes the program to identify a large number of voxels in this region as air instead of lung tissue.

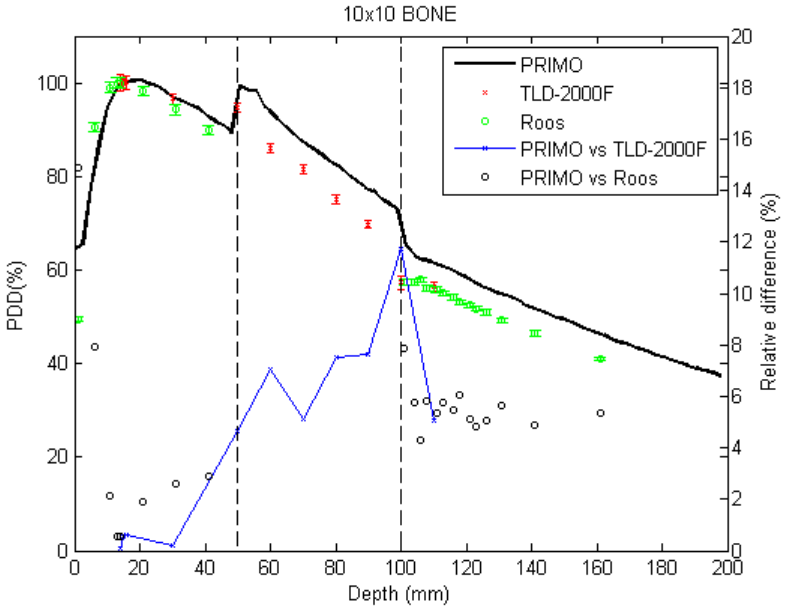

Figure 5.10: PDD's obtained for 6 MV and $10x10\ cm^2$ photon beam using the calibration curve and material assignment by default in PRIMO for the bone phantom.

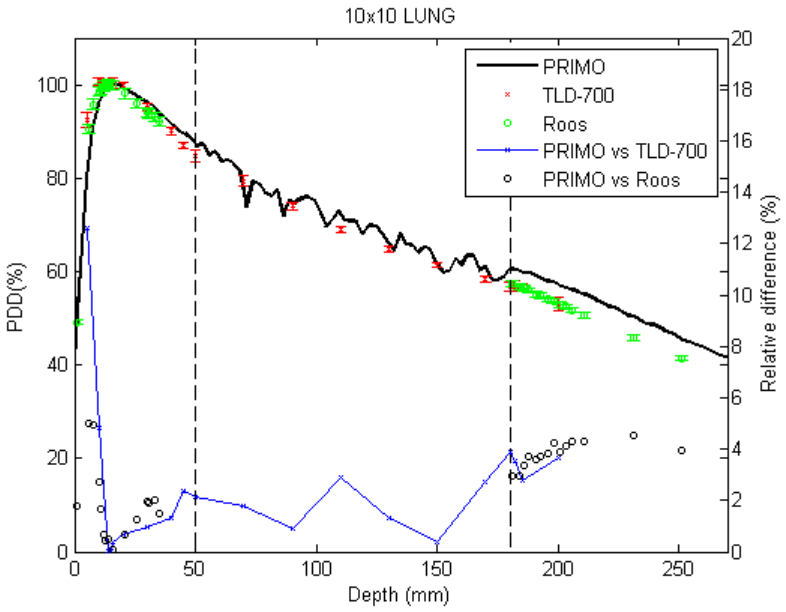

Figure 5.11: PDD's obtained for 6 MV and $10x10\ cm^2$ photon beam using the calibration curve and material assignment by default in PRIMO for the lung phantom.

5.3.2 Simulations with CT parameters adjusted

After adjusting the CT calibration curve and the material assignment different field sizes have been simulated for both experimental setups. Figures 5.12, 5.13 and 5.14 show the results obtained for the lung-equivalent phantom. Results in bone equivalent phantom are shown in figures 5.15 and 5.16.

For the lung-equivalent heterogeneity phantom, simulation results obtained with $2x2$ cm^2 and $10x10\ cm^2$ fields show a reasonable agreement with the experimental results. A part from the build-up region, differences over 4% in dose are also found in a few specific points. For the $2x2\ cm^2$ field we find a point with a dose difference over 5% in the boundary between the two medias where the curve presents a high dose gradient as well as the fact that the voxel size does not allow the program to generate accurate results in zones adjacent to a material change. In the simulation results with the $10x10\ cm^2$

we observe a few points in the region underneath the heterogeneity with dose difference slightly greater than 4%.

On the other hand simulation results for the $5x5\ cm^2$ field show larger discrepancies in the heterogeneity region where differences are over 5% in most of the points. Results in the rest of the phantom are in good agreement with experimental measurements except for a few points in the region underneath the heterogeneity where we find discrepancies over 4%.

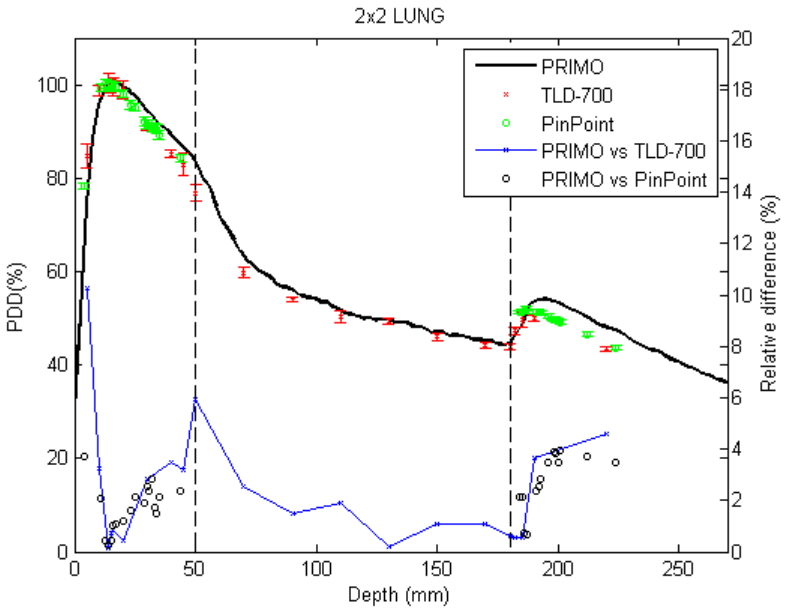

Figure 5.12: PDD curves on the slab phantom with the lung-equivalent heterogeneity using a $2 \times 2\ cm^2$ field size.

Results obtained in the bone-equivalent phantom with the $5x5\ cm^2$ field present dose discrepancies between the tolerance levels except in the heterogeneity region where we find differences over 5%. For the $10x10\ cm^2$ field we find dose differences over 4% in all points of the heterogeneity region and the region underneath the heterogeneity. Largest discrepancies are found in the boundary between the bone-equivalent region and the region underneath.

Dose profiles obtained inside the heterogeneous region for the bone-equivalent heterogeneity phantom and the lung-equivalent heterogeneity phantom are depicted in figures

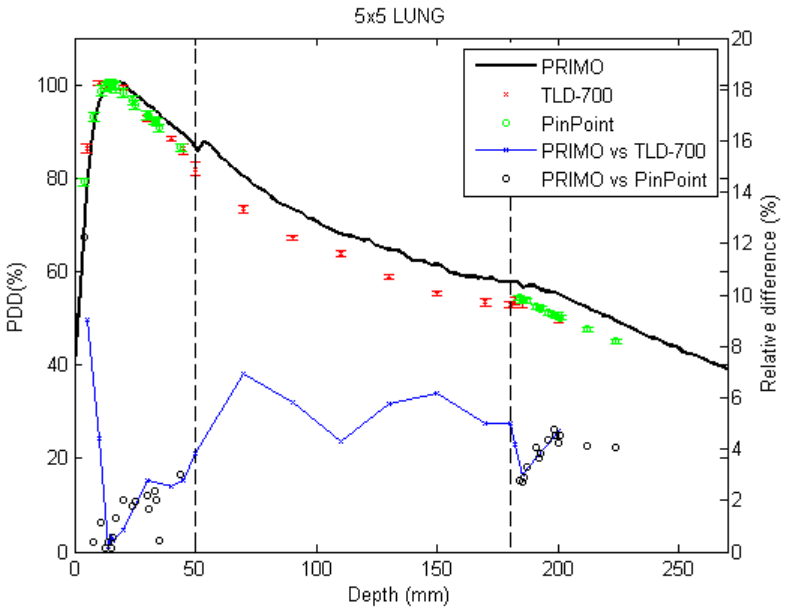

Figure 5.13: PDD curves on the slab phantom with the lung-equivalent heterogeneity using a $5 \times 5\ cm^2$ field size.

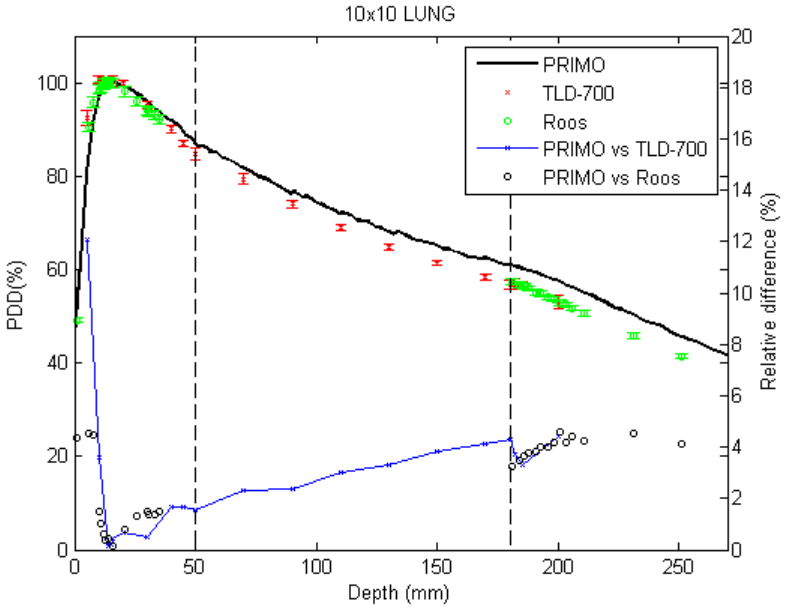

Figure 5.14: PDD curves on the slab phantom with the lung-equivalent heterogeneity using a $10 \times 10\ cm^2$ field size.

5.17 and 5.18 respectively. In both setups we observe a tendency of the algorithm to widen the dose profile. Nevertheless one must take into account two main reasons that

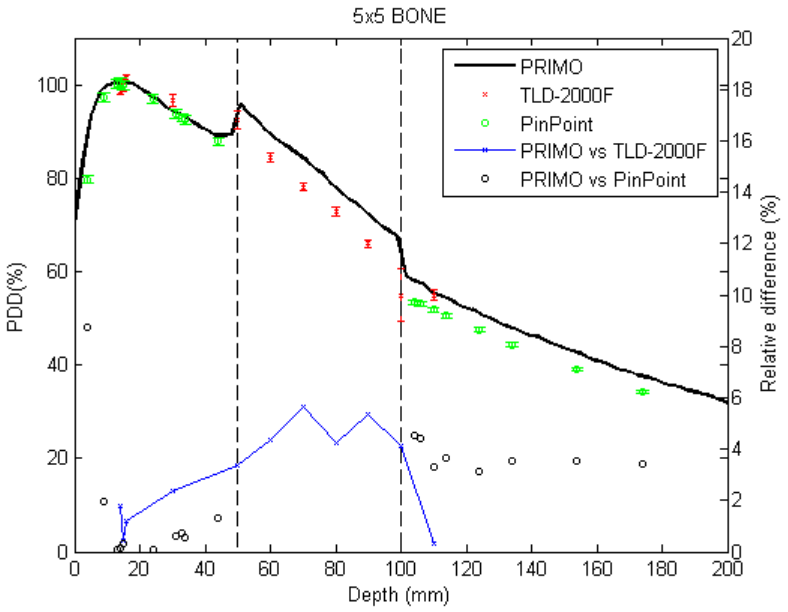

Figure 5.15: PDD curves on the slab phantom with the bone-equivalent heterogeneity using a $5 \times 5\ cm^2$ field size.

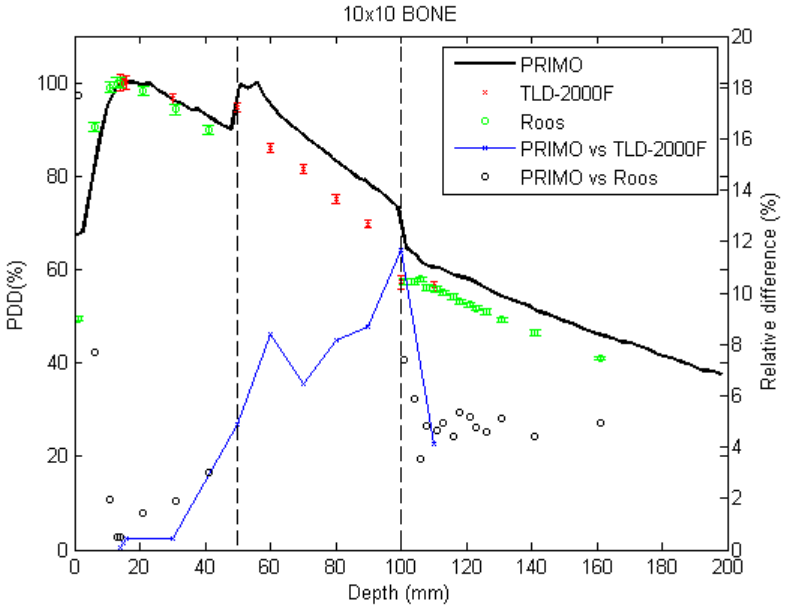

Figure 5.16: PDD curves on the slab phantom with the bone-equivalent heterogeneity using a $10 \times 10\ cm^2$ field size.

make difficult to obtain accurate dose profiles in this conditions. First the voxel size which is given by the CT image causes the profile to be represented with a short amount

of voxels in the central beam axis region. In addition discrepancy sources associated to the fact that dose is calculated in a CT image instead of in a geometrical phantom take a relevant role (artifacts generated in the CT image acquisition and errors generated in the subsequent identification of each voxel by the algorithm from the image).

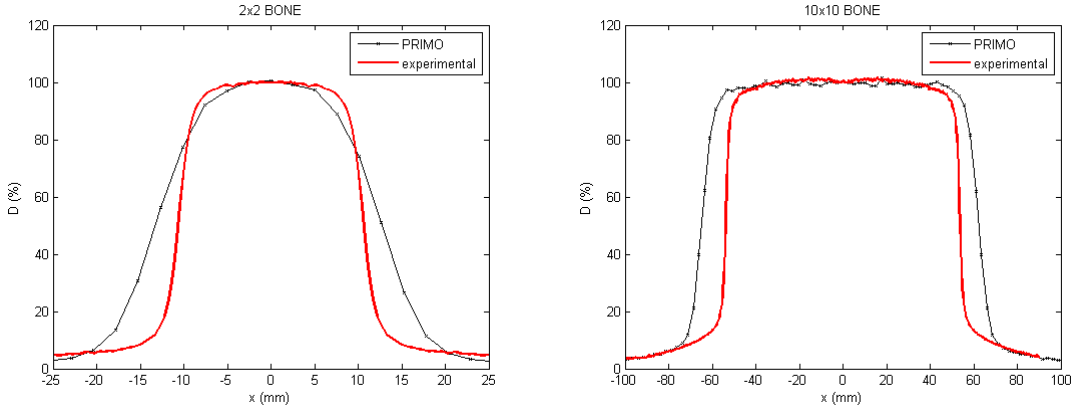

Figure 5.17: Dose profiles in the slab phantom with the bone-equivalent heterogeneity.

Experimental and simulated beam penumbraes are shown in table 5.5. In the lung-equivalent heterogeneity phantom the differences are about 2 millimeters for all field sizes while in the bone-equivalent heterogeneity phantom discrepancies are of 3 millimeters and above.

	Lung		Bone	
Field size	EBT	PRIMO	EBT	PRIMO
$2 \times 2cm^2$	7.6	9.7	3.1	7.1
$5 \times 5cm^5$	10.7	12.7	-	-
$10 \times 10\ cm^2$	12.6	14.2	4.3	7.8

Table 5.5: Beam penumbrae (in mm) for the different simulations and measured with EBT radiochromic films

Table 5.6 show the simulation times elapsed for each case in this set of simulations. In this case all simulations were run using the two core Intel ® Core^{TM} 2 duo processor.

Figures 5.19 and 5.20 show the PDD curves obtained when simulating a $5 \times 5\ cm^2$ field

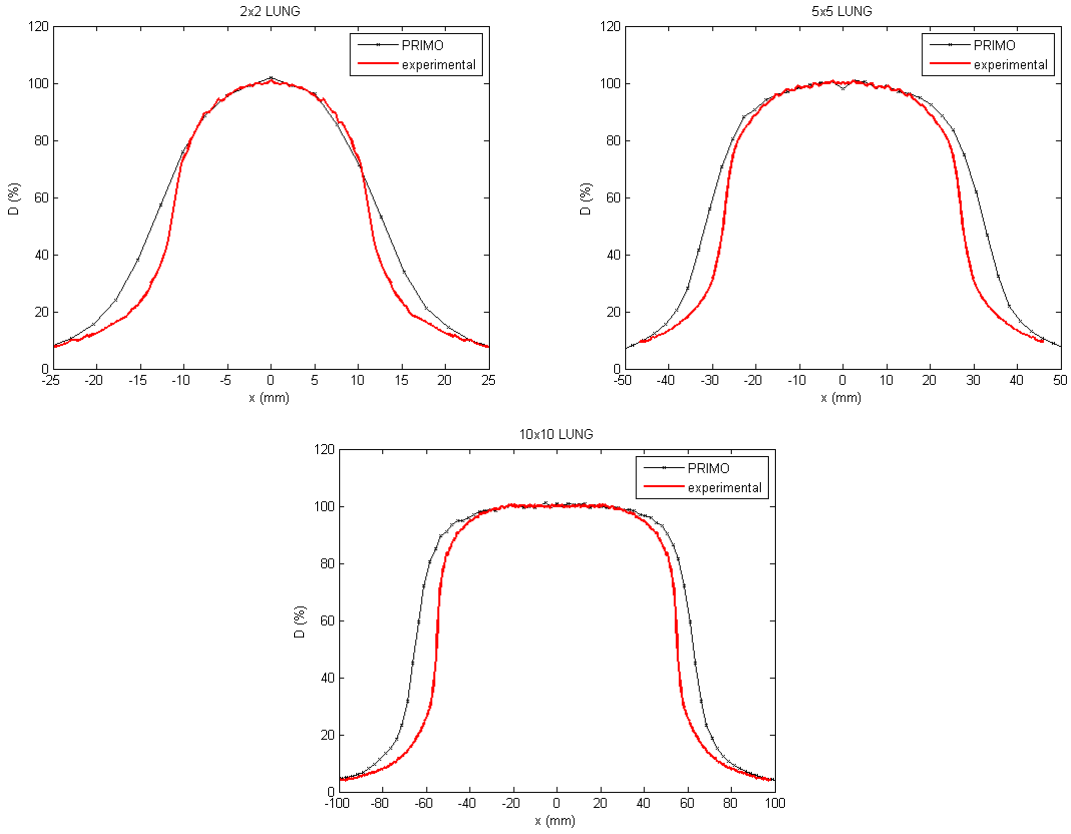

Figure 5.18: Dose profiles in the slab phantom with the lung-equivalent heterogeneity.

Field size	histories		S1	S2	S3
$2 \times 2\ cm^2$	$1.25 \cdot 10^8$	Bone	22.7	1	5.8
		Lung			3.1
$5 \times 5\ cm^2$	$1.25 \cdot 10^8$	Bone	21.4	1.5	30.3
		Lung			18.4
$10 \times 10\ cm^2$	$2.25 \cdot 10^8$	Bone	63.9		115.5
		Lung			77.5

Table 5.6: Elapsed times in hours in the simulation of the different segments.

in the studied setups using water instead of muscle and cartilage in the material list. In the heterogeneous region we observe a better agreement with experimental results than in previous simulations for both setups. Otherwise in the rest of phantom, results are similar to those in previous simulations. In this case dose differences are below 4% along the entire

curve except for the build up region in both configurations. Average discrepancies are 0.6% lower compared to those in previous simulations. Figure 5.21 show the dose profile obtained in the lung region. Results are similar than the previous simulation.

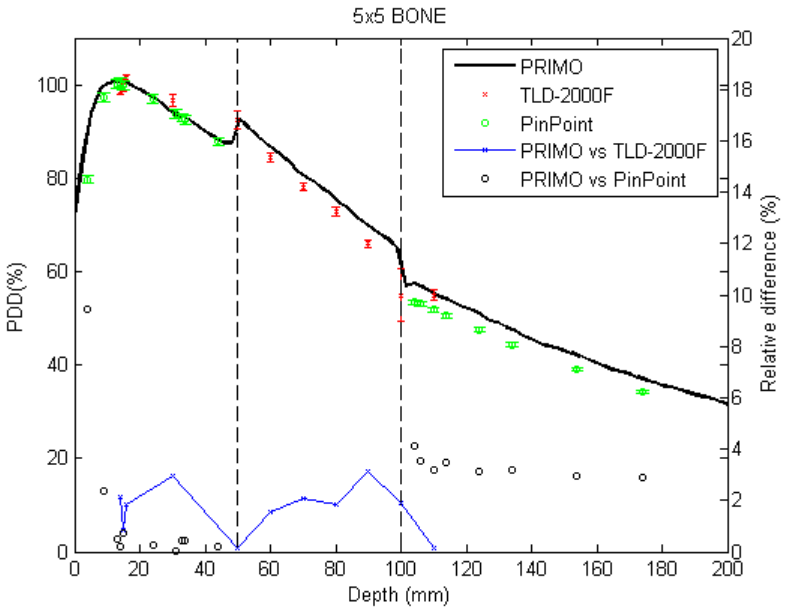

Figure 5.19: PDD curves obtained for the $5 \times 5\ cm^2$ field in the bone-equivalent heterogeneity phantom using water instead of muscle and cartilage in the material list.

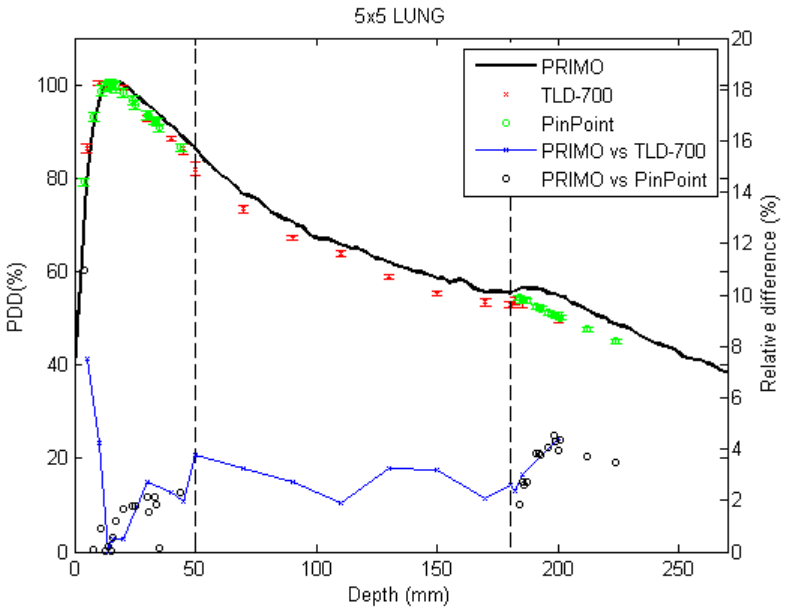

Figure 5.20: PDD curves obtained for the $5 \times 5\ cm^2$ field in the lung-equivalent heterogeneity phantom using water instead of muscle and cartilage in the material list.

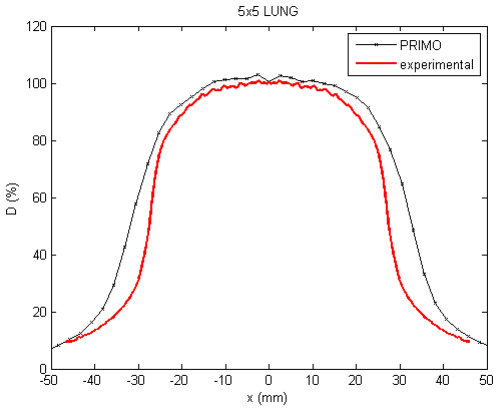

Figure 5.21: Dose profile obtained in the slab phantom with the lung-equivalent heterogeneity with a $5 \times 5\ cm^2$ field and replacing the muscle and cartilage of the material list by water.

5.3.3 Simulations with geometrical phantoms

PDD curves obtained when modelling geometrical phantoms are shown in figures 5.22, 5.23 and 5.24 for the lung heterogeneity. PDD curves in the bone heterogeneity phantom are presented in figures 5.25 and 5.26. Results have been compared with those obtained with CT images as well as the experimental measurements. Results obtained with the geometrical phantoms are in better agreement along the whole PDD curve. Dose calculations in the region underneath the heterogeneity are clearly more accurate with the geometrical phantom on every one of the configurations. Dose differences between experimental measurements and results obtained with geometrical phantoms lower than 4% throughout the PDD curves except in the lung region for the $2 \times 2\ cm^2$ field.

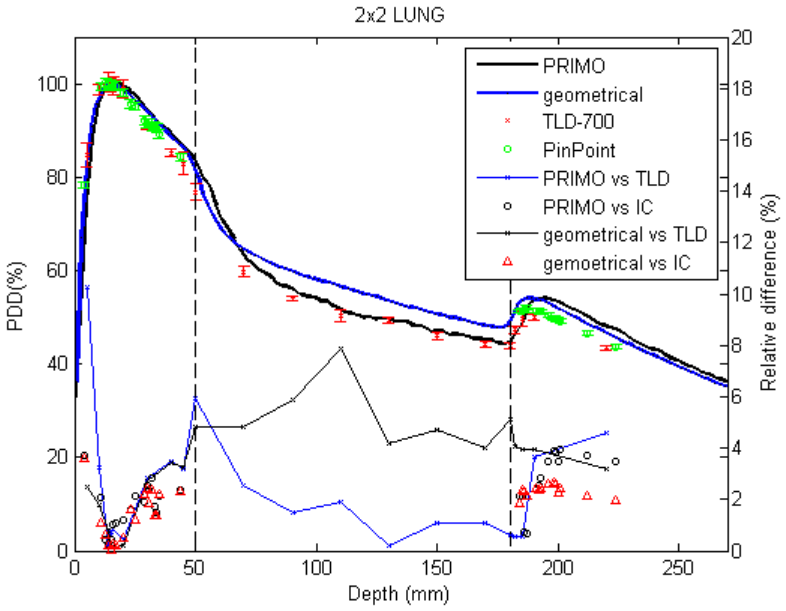

Figure 5.22: PDD curve in the slab phantom with the lung-equivalent heterogeneity using a $2 \times 2\ cm^2$ field size.

Figures 5.27 and 5.28 show the dose profiles obtained inside the heterogeneous region. Again results obtained in this case are in better agreement than the results obtained with CT images and they are reasonably accurate except for the $2 \times 2\ cm^2$ field inside the bone region.

Table 5.3.3 show the experimental and simulated lateral penumbraes. Discrepancies

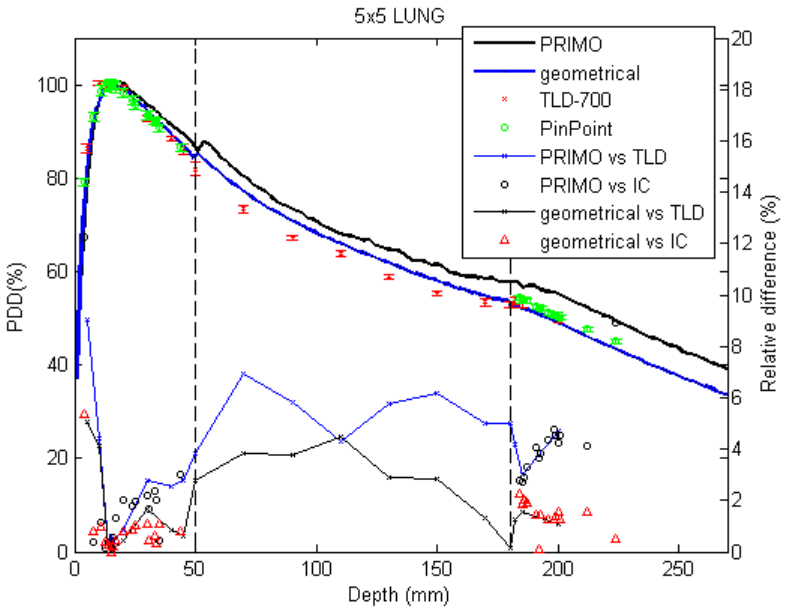

Figure 5.23: PDD curves in the slab phantom with the lung-equivalent heterogeneity using a $5 \times 5\ cm^2$ field size.

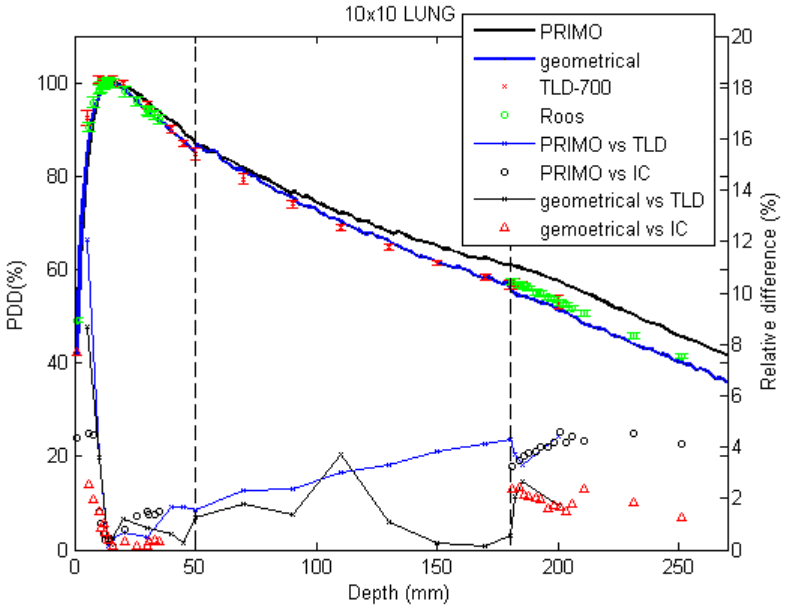

Figure 5.24: PDD curves in the slab phantom with the lung-equivalent heterogeneity using a $10 \times 10\ cm^2$ field size.

between measurements and simulations are below 3 millimeters in all configurations except for the bone-equivalent heterogeneity with a $2 \times 2 cm^2$ field.

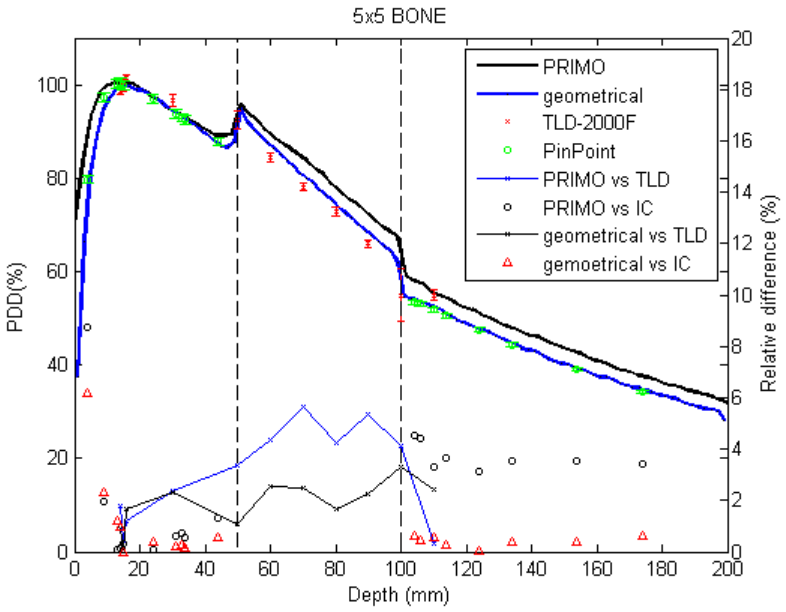

Figure 5.25: PDD curves in the slab phantom with the bone-equivalent heterogeneity using a $5 \times 5\ cm^2$ field size.

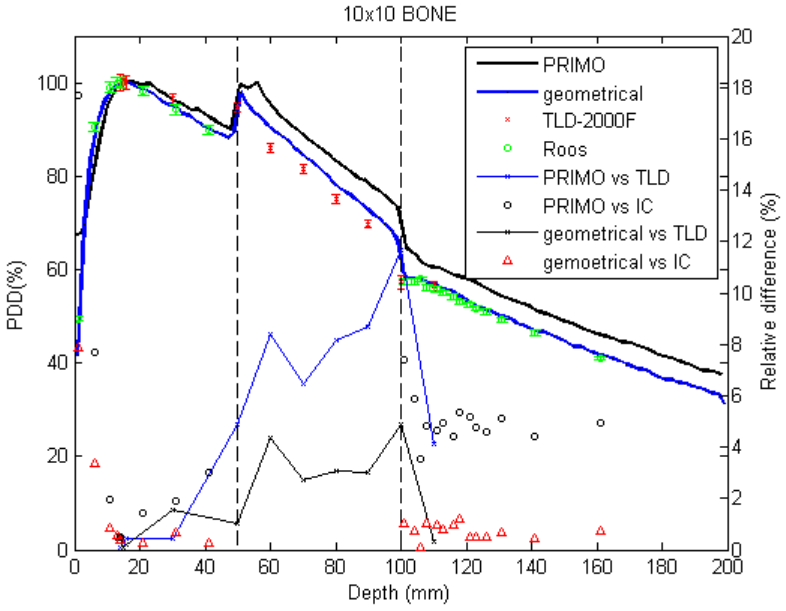

Figure 5.26: PDD curves in the slab phantom with the bone-equivalent heterogeneity using a $10 \times 10\ cm^2$ field size.

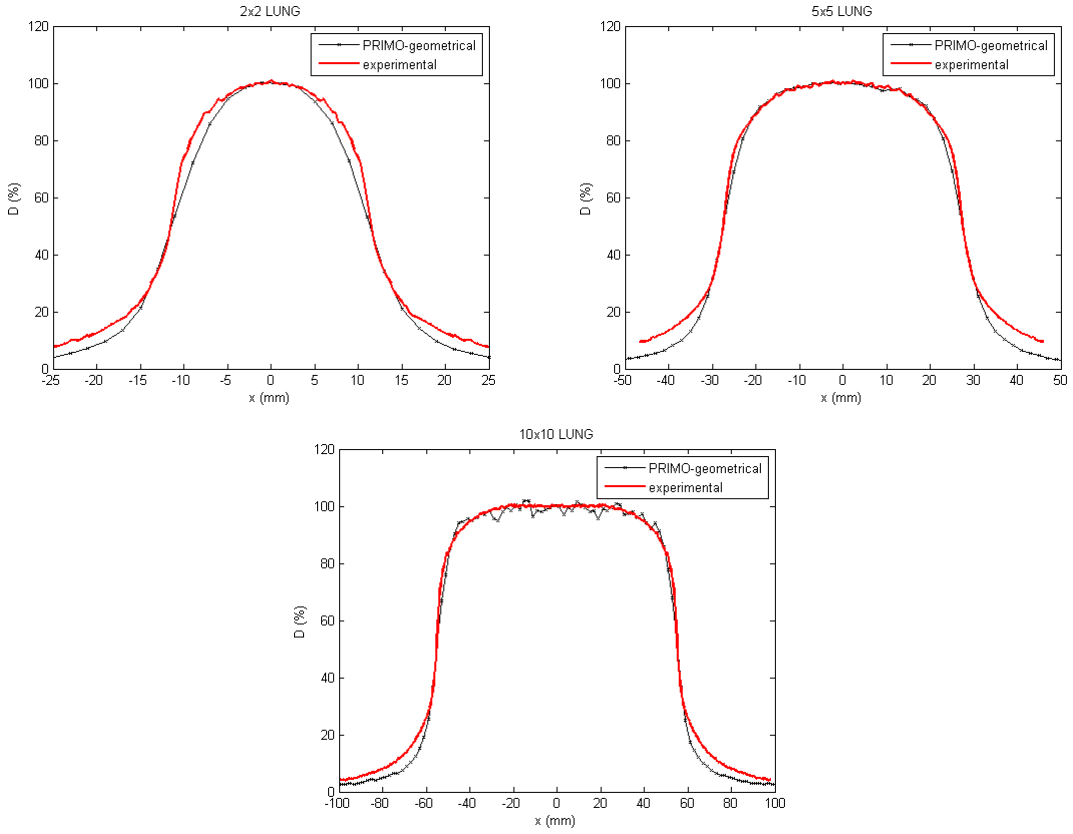

Figure 5.27: Dose profiles in the slab phantom with the lung-equivalent heterogeneity.

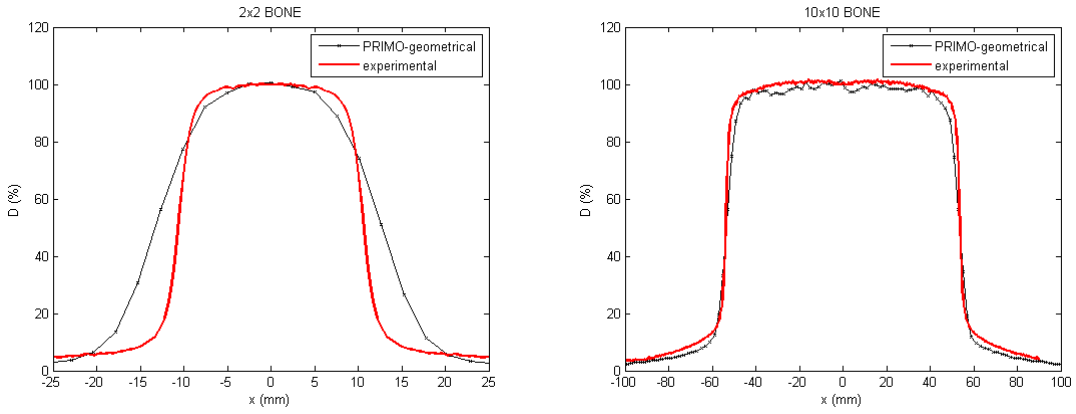

Figure 5.28: Dose profiles in the slab phantom with the bone-equivalent heterogeneity.

5.3.4 Conclusions on the performance of the algorithm in the presence of heterogeneities

Results in previous sections show that dose distributions in geometries with heterogeneous regions can be generated with reasonably good accuracy by the algorithm. When dose

	Lung		Bone	
Field size	EBT	PRIMO-geom.	EBT	PRIMO-geom.
$2 \times 2cm^2$	7.6	7.4	3.1	7.1
$5 \times 5cm^5$	10.7	9.3	-	-
$10 \times 10\ cm^2$	12.6	10.2	4.3	6.7

Table 5.7: Beam penumbrae (in mm) for the different simulations with geometrical phantoms and measured with EBT radiochromic films

distribution is calculated on CT images the algorithm proved to be very sensitive to the material identification and the CT calibration curve. Special care must be taken with these parameters when simulating with CT images.

On the other hand it has been shown that phase space files generated with PRIMO allow to produce very accurate dose distributions in geometrical phantoms even in the presence of heterogeneities. Besides simulations with geometrical phantoms showed on average discrepancies 1.5% lower than simulations on CT images.

Chapter 6

Conclusions

Results showed that the PRIMO code allows to obtain accurate dose distributions in water phantoms.99% of points in the PDD curves calculated by the algorithm passed the gamma test in all simulations and discrepancies were below 2% along the curves except in the first millimeters of the phantom where discrepancies can be attributable to deficiencies of the experimental measurements. Calculations of dose profiles were in reasonably good agreement with experimental measurements although further investigation would be needed to evaluate the performance of the algorithm.

PSF files generated at the downstream end of the linac by PRIMO allowed to obtain very accurate results in the build up region. The average dose differences found between simulations and experimental results were below 2% for the two studied beam energies.

Dose calculations on CT images of heterogeneous phantoms were in reasonably good agreement with experimental results. Average discrepancies below 4% were found in all simulations except for one case. Nevertheless the algorithm proved to be very sensitive to the CT parameters adjustment. Results in dose profiles inside heterogeneous regions were reasonably accurate. Furthermore PSF files generated at the downstream end of the linac allowed to obtain very accurate results in heterogeneous geometrical phantoms.

Bibliography

[1] World Health Organization (WHO). Globocan. Technical report, Tech. Rep. (International Agency for Research on Cancer (IARC)), 2012.

[2] International Atomic Energy Agency. Relative biological efectiveness in ion beam therapy. Technical Report 46, IAEA, Viena, 2008.

[3] Arthur J Olch, Lee Gerig, Heng Li, Ivaylo Mihaylov, and Andrew Morgan. Dosimetric effects caused by couch tops and immobilization devices: report of AAPM Task Group 176. *Medical physics*, 41(6):061501, June 2014.

[4] Antonella Fogliata, Eugenio Vannetti, Dirk Albers, Carsten Brink, Alessandro Clivio, Tommy Knöös, Giorgia Nicolini, and Luca Cozzi. On the dosimetric behaviour of photon dose calculation algorithms in the presence of simple geometric heterogeneities: comparison with Monte Carlo calculations. *Physics in medicine and biology*, 52(5):1363–1385, 2007.

[5] Indrin J. Chetty, Bruce Curran, Joanna E. Cygler, John J. DeMarco, Gary Ezzell, Bruce a. Faddegon, Iwan Kawrakow, Paul J. Keall, Helen Liu, C.-M. Charlie Ma, D. W. O. Rogers, Jan Seuntjens, Daryoush Sheikh-Bagheri, and Jeffrey V. Siebers. Report of the AAPM Task Group No. 105: Issues associated with clinical implementation of Monte Carlo-based photon and electron external beam treatment planning. *Medical Physics*, 34(12):4818, 2007.

[6] Marta Bueno Vizcarra. *Absorbed dose assessment in the presence of tissue heterogeneities in external radiotherapy.* PhD thesis, UPC, 2013.

[7] N Papanikolaou, JJ Battista, and AL Boyer. Tissue inhomogeneity corrections for megavoltage photon beams. *AAPM Task Group*, (85), 2004.

[8] International Commission on Radiation Units (ICRU). Determination of absorbed dose in a patient irradiated by beams of X or gamma rays in radiotherapy procedures. Technical report, Bethesda, 1976.

[9] Ben Mijnheer, Olszewska Agnieszka, Claudio Fiorino, Tommy Knöös, Jean-Claude Rosenwald, and Hans Welleweerd. QUALITY ASSURANCE OF TREATMENT PLANNING SYSTEMS NON-IMRT PHOTON BEAMS QUALITY ASSURANCE OF TREATMENT PLANNING SYSTEMS PRACTICAL EXAMPLES FOR NON-IMRT PHOTON BEAMS.

[10] D a Low, W B Harms, S Mutic, and J a Purdy. A technique for the quantitative evaluation of dose distributions. *Medical physics*, 25(5):656–61, May 1998.

[11] J. M. Fernández-Varea F. Salvat and J. Sempau. *PENELOPE-2011 : A Code System for Monte Carlo Simulation of Electron and Photon Transport*. Number July. Issy-les-Moulineaux, France, 2011.

[12] J Baro and J Sempau. PENELOPE: an algorithm for Monte Carlo simulation of the penetration and energy loss of electrons and positrons in matter. *Nuclear Instruments and Methods in Physics Research*, (95), 1995.

[13] M Rodriguez, J Sempau, and L Brualla. PRIMO: a graphical environment for the Monte Carlo simulation of Varian and Elekta linacs. *Strahlentherapie und Onkologie : Organ der Deutschen Röntgengesellschaft ... [et al]*, 189(10):881–6, October 2013.

[14] Raul Camats Domínguez. *Medida de la dosis en piel en radioterapia externa mediante dosímetros TL ultrafinos*. Proyecto final de master, UPC, 2014.

[15] Hui Khee Looe, Dietrich Harder, and Björn Poppe. Experimental determination of the effective point of measurement for various detectors used in photon and electron beam dosimetry. *Physics in Medicine and Biology*, 56(14):4267, 2011.

[16] José M Fernández-Varea, Pablo Carrasco, Vanessa Panettieri, and Lorenzo Brualla. Monte Carlo based water/medium stopping-power ratios for various ICRP and ICRU tissues. *Physics in medicine and biology*, 52(21):6475–83, November 2007.

[17] A E Nahum J V Siebers, P J Keall and R Mohan. Converting absorbed dose to medium to absorbed dose to water for Monte Carlo based photon beam dose calculations. *Physics in medicine and biology*, 983(45):983–995, 2000.

[18] Josep Sempau and Andreu Badal. *PenEasy, aa modular main program and voxelized geometry package (v.2008-06-15)*. 2005.

[19] L Brualla, F Salvat, and R Palanco-Zamora. Efficient Monte Carlo simulation of multileaf collimators using geometry-related variance-reduction techniques. *Physics in medicine and biology*, 54(13):4131–49, July 2009.

[20] L. Brualla and W. Sauerwein. On the efficiency of azimuthal and rotational splitting for Monte Carlo simulation of clinical linear accelerators. *Radiation Physics and Chemistry*, 79(9):929–932, September 2010.

[21] M Rodriguez, J Sempau, and L Brualla. A combined approach of variance-reduction techniques for the efficient Monte Carlo simulation of linacs. *Physics in medicine and biology*, 57(10):3013–24, May 2012.

[22] Josep Sempau, Andreu Badal, and Lorenzo Brualla. A PENELOPE-based system for the automated Monte Carlo simulation of clinacs and voxelized geometries-application to far-from-axis fields. *Medical physics*, 38(11):5887–95, November 2011.

Appendix A

Variance-reduction techniques

MC simulations of linacs is very inefficient, particularly the simulation of radiation transport in linac targets. In these structures, electrons are transported through materials with high atomic number in order to produce bremsstrahlung photons. Furthermore, photons are emitted in all directions and only a fraction of them are directed at the bottom of the accelerator and are useful for dose calculations; the rest are absorbed in the linac head components or exit the geometry. Thus, the use of variance-reduction techniques is mandatory to reduce the simulation times to clinically acceptable values.

A set of variance-reduction techniques are implemented in PRIMO [19, 20, 21, 22]. These techniques are briefly described below:

- **Interaction forcing**: It consists in artificially increasing the interaction cross section of a certain interaction mechanism and material. To avoid a bias in the simulation results, the statistical weight of descendent particles produced in forced interactions is reduced. This technique is particularly useful and allows to obtain better statistics when simulating particles travelling through thin material layers or low density materials.
- **Range rejection**: Charged particles that have travelled far away from the zone of interest and have a negligible chance of contributing to the tallied quantities are discarded to avoid loosing computation time while simulating them.

- **Russian roulette**: Particles whose probability to contributing to the tallied quantities is low, or whose contribution to the tallied quantities will be low due to a low statistical weight are eliminated from the simulation with a probability $K < 1$. In order to keep the simulation unbiased, particles that survive have their weight increased by a factor $1/(1 - K)$.

- **Splitting**: A particle with a large probability of contributing to the tallied quantities is split, this means that a particle, with statistical weight w_0 and in a certain state, is transformed in a number $S > 1$ of identical particles with weights $w = w_0/S$ in the same state.

- **Rotational splitting**: It is applied to particles travelling through geometries with cylindrical symmetry when the primary source has also the same kind of symmetry. This is the case of Varian Clinacs from the primary source downstream to the ionisation chamber. It is a kind of splitting in which each split particle is rotated about the central beam axis an azimuthal angle. The particle direction cosines of each replica are transformed in order to keep the direction of the original particle relative to the central beam axis.

- **Splitting-roulette**: In splitting-roulette, Russian roulette and splitting techniques are combined. When a particle tends to move away from the region of interest is subjected to Russian roulette and if it survives their descendants are split.

- **Movable skin**: The movable-skin method consists of defining relevant zones of the geometry in which an accurate transport of radiation is performed, whereas in less relevant zones the transport of some particles is discontinued.